Marine Geology 430 (2020) 106343

Contents lists available at ScienceDirect

Marine Geology

journal homepage: www.elsevier.com/locate/margo

Invited Research Article

Detecting shifts of submarine sediment boundaries using side-scan mosaics and GIS analyses

Daphnie S. Galvez[a,*], Svenja Papenmeier[a,c], H. Christian Hass[a], Alexander Bartholomae[b], Vera Fofonova[a], Karen Helen Wiltshire[a]

[a] Alfred Wegener Institute, Helmholtz Centre for Polar and Marine Research, Wadden Sea Research Station, Hafenstraße 43, 25992 List, Germany
[b] Senckenberg am Meer, Südstrand 40, 26382 Wilhelmshaven, Germany
[c] Leibniz Institute for Baltic Sea Research Warnemünde, Seestraße 15, 18119 Rostock, Germany

ARTICLE INFO

Keywords:
Side-scan sonar
Change detection
GIS
Seafloor-mapping
Sediment shifts
Lag deposits
Sedimentology

ABSTRACT

Detecting changes of sediment boundaries on the seafloor is important for a better understanding of sediment dynamics and related impacts to benthic habitats. Side-scan sonars (SSS) perform more cost-effectively in shallow waters than other acoustic systems because of their larger swath widths, and the resolution of its images does not change with varying water depth. However, as they are generally towed behind the survey vessel, they tend to have lower positioning accuracy, which makes them unreliable for change detection analyses. In this study, we present a workflow that processes SSS data in a way that makes them fit for change detection analyses. To test the capacity of SSS mosaics for change detection, we used a free software called "Digital Shoreline Analysis System", which was developed by the United States Geological Survey for ArcGIS version 10.4 onwards. The methods were applied in three areas in the Sylt Outer Reef, German Bight, North Sea. Our results showed that with appropriate processing, SSS mosaics could be used for change detection of sharp sediment boundaries. We found a common trend in the sediment distribution patterns of coarse sediments by monitoring the movement of their boundaries. The boundaries moved in northeast-southwest direction and boundary movements of less than 20 m were typically observed. The methods presented here are semi-automated, repeatable, and replicable, which has potential for wide-scale monitoring of sediment distribution patterns.

1. Introduction

Monitoring changes in sediment distribution pattern is important to understand the spatio-temporal patterns of environmental processes and the impact of human activities in the past decades (Auster et al., 1996; Rijnsdorp et al., 2020; Rumohr and Kujawski, 2000). Seafloor sediments influence microenvironmental conditions that in turn have an important impact on meiofaunal communities (Gibbons, 1988). Moreover, it has been proposed that sediment disturbances by anthropogenic activities interfere with biological controls of sediment dynamics and have caused major changes in the functioning of soft-bottom ecosystems (Eriksson et al., 2010). Therefore, comprehensive monitoring of marine sedimentary ecosystems has been recommended to quantify large-scale and cumulative effects of anthropogenic impacts and to protect the sedimentary ecosystem (Heery et al., 2017). In this regard, detecting sediment shifts is important to locate and to monitor the impacts of sedimentological changes to benthic habitats, marine ecosystem services, and sediment dynamics on the seafloor (Eriksson et al., 2010; Montereale-Gavazzi et al., 2018; Thistle et al., 1985; Troell et al., 2005).

Remote sensing through acoustic technologies is often used to provide information on seafloor morphology, sediment types, and sediment dynamics (Pau and Hammer, 2013; Van Lancker and Baeye, 2015). Acoustic technologies for seafloor-monitoring include towed Side-Scan Sonar (SSS) systems, Multibeam Echosounder Systems (MBES), and Acoustic Ground Discrimination Systems (AGDS). SSS is sometimes preferred for sediment characterization because of its higher backscatter resolution than MBES backscatter data (Lucas et al., 2020; Michaelis et al., 2019b; Subarsyah and Arifin, 2019). It is also ideal for large-scale seafloor monitoring because of its large swath widths and adjustable rope length of the tow-fish (Greene et al., 2018; Papastamatiou et al., 2020).

However, an important drawback of SSS is its lack of secondary information regarding bathymetry and angular dependency of

* Corresponding author.
E-mail addresses: daphnie.galvez@awi.de, daphniegalvez@gmail.com (D.S. Galvez), svenja.papenmeier@io-warnemuende.de (S. Papenmeier), Christian.Hass@awi.de (H.C. Hass), alexander.bartholomae@senckenberg.de (A. Bartholomae), Karen.Wiltshire@awi.de (K.H. Wiltshire).

https://doi.org/10.1016/j.margeo.2020.106343
Received 13 November 2019; Received in revised form 10 September 2020; Accepted 14 September 2020
Available online 19 September 2020
0025-3227/

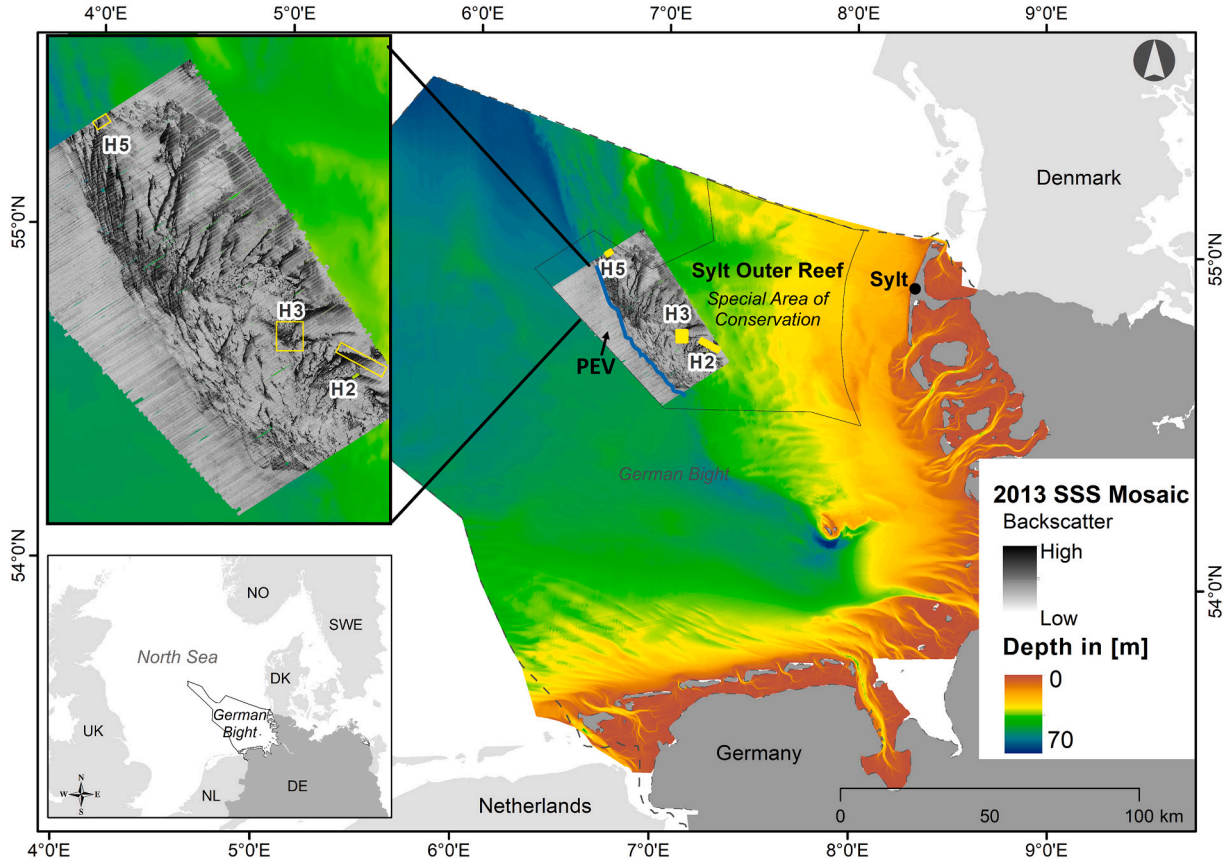

Fig. 1. The study areas are located in the Sylt Outer Reef and approximately 70 km away from the Island of Sylt, Germany. The SSS mosaic was derived from our 2013 acoustic survey with a grid resolution of 1 m (Papenmeier and Hass, 2018). The blue line marks the eastern boundary of the Paleo Elbe Valley. (For interpretation of the references to color in this figure legend, the reader is referred to the web version of this article.)

returning echoes, which prohibits accurate correction of radiometric and geometric distortions (Fakiris et al., 2018). Radiometric distortion in SSS images is caused mainly by transmission losses, sonar altitude (Capus et al., 2004), beam patterns, angular responses of different sediments, and topography changes (Blondel, 2010; Zhao et al., 2017). Geometric distortion occurs when the flat bottom assumption is not valid and the pixels are mapped incorrectly in the image frame, yielding distorted representations of the seafloor (Cervenka et al., 1994). In addition, since SSS are generally towed behind the survey vessel, they tend to have lower positioning accuracy. These distortions may affect the accuracy of change detection analyses and may produce misleading information. Thus, it is necessary to correct the SSS data before conducting change detection analysis.

Geocoder is a software tool that implements radiometric and geometric corrections to acoustic backscatter acquired by MBES and SSS (Fonseca and Calder, 2005). The software was implemented in a number of commercial software suites such as the *Fledermaus Geocoder Toolbox* (FMGT), which is a module of the commercial *Fledermaus* software from QPS (Schimel et al., 2015). FMGT has been commonly used in various studies to process multibeam backscatter data (Eidem et al., 2017; Ierodiaconou et al., 2018; Montereale-Gavazzi et al., 2018), but only few have used it for SSS data (Fakiris et al., 2018).

SSS images have been used to detect changes in submarine features such as sorted bedforms, sand dunes, and sand waves (Anthony and Leth, 2002; Franzetti et al., 2013; Goff et al., 2005; Van Lancker et al., 2004). Several techniques have been presented to detect changes using SSS imagery. One approach is to digitize the outline of the features (e.g. rippled scour depressions) into polygons and compare the changes of their areal extent using time-series SSS imagery (Rosenberger et al., 2019). Another method presented is to delineate the boundary lines that divide two major sediment types or where there is an abrupt change in grey-scale contrast in the SSS mosaic (Diesing et al., 2006). These methods were able to detect and measure changes using SSS mosaics, but detailed quantification of the changes were lacking.

The German Bight is situated in the southeastern North Sea, a young and shallow continental shelf sea, and the majority of its seafloor is composed of Holocene marine sand on top of Pleistocene lag deposits. These lag deposits and other coarse sediment (e.g. well-sorted coarse sand and gravel) can be discriminated from the surrounding finer sediment by a very sharp boundary line or as a gradual change from low to high backscatter intensity. This boundary line can easily be identified in SSS mosaics where it is represented by an abrupt shift from low to high backscatter (light to dark colors in this study) (Diesing et al., 2006; Mielck et al., 2015; Papenmeier et al., 2020; Papenmeier and Hass, 2018). This boundary shows potential for monitoring sediment shifts if the positioning is accurate, because shifts in the position of the boundary over time suggest shifts of the coarse and fine sediment domains involved. The term 'boundary' in this paper, refers to the boundary line that separates high from low backscatter zones, which are interpreted as zones of coarser and finer sediment.

In this study, we present a workflow that detects and quantifies spatio-temporal changes of the sediment boundaries using SSS and Geographic Information Systems (GIS). To this end, we monitored the sharp sediment boundaries at the northwestern Sylt Outer Reef (SOR) within the German Bight to examine changes in sediment cover between 2016 and 2018. We selected three focus areas (H2, H3, H5) within the SOR which differ in sediment distribution and boundary pattern. Specifically, the objectives of the study were: (1) to enhance the quality of SSS mosaics towards allowing semi-automated image classification, (2) to create comparable mosaics for change detection,

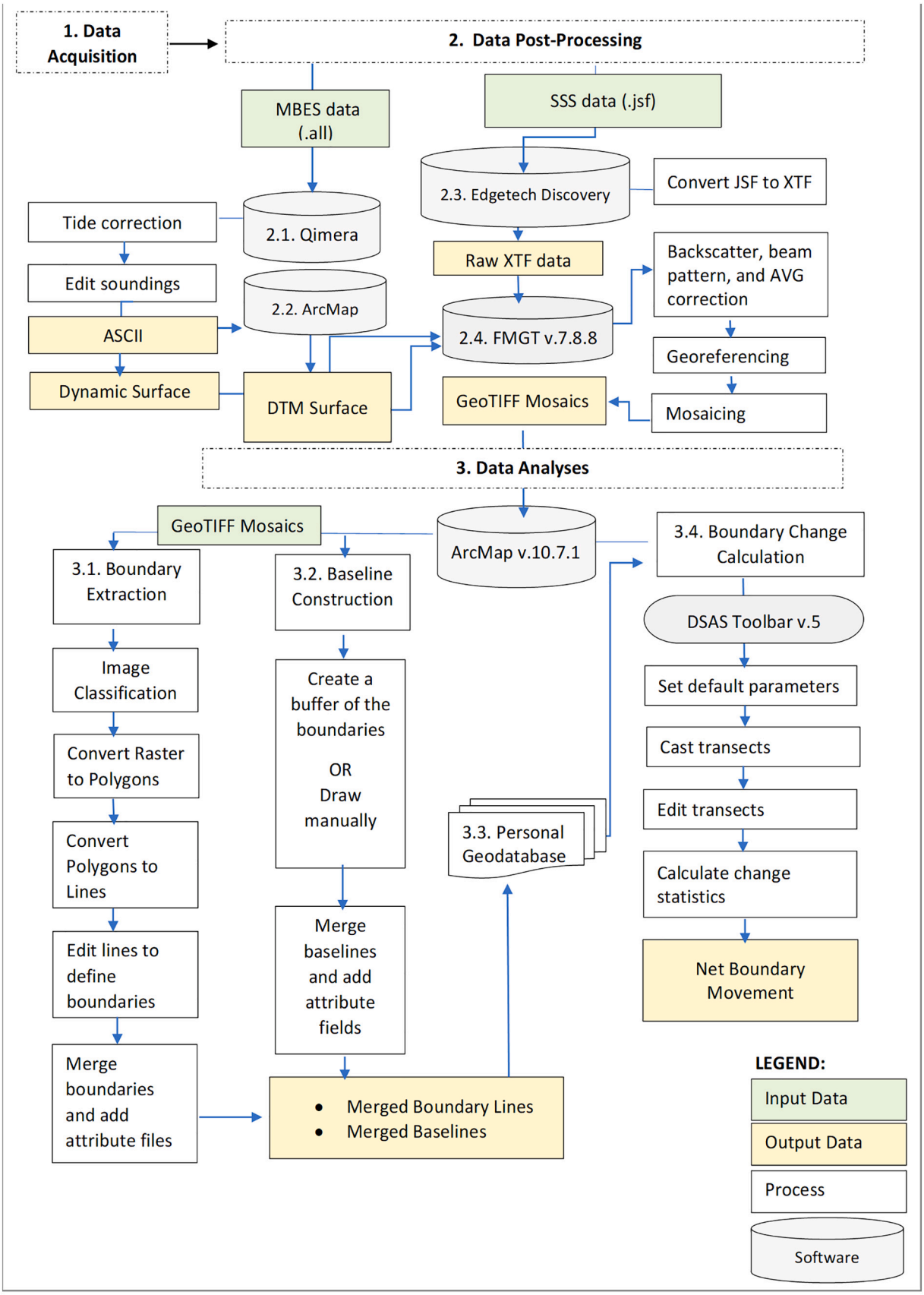

Fig. 2. Data processing and analysis workflow to detect shifts of sediment boundaries.

Table 1
Date and settings of offshore surveys with FS Heincke. HSM LF stands for High Speed Mode Low Frequency. Survey settings for each focus area were specified in the last column.

Cruise number	Date	Data type	Survey settings
HE 474 (H3 only)	12–20 Oct 2016	Backscatter	Edgetech 4200 SSS 300 kHz, HSM LF 75 m range
		Bathymetry	Kongsberg EM710 MBES: Transmit mode: Very Shallow Frequency range: CW 65–105 kHz Pulse length [msec]: 0.2 Swath width = 90 °
HE 501	15–28 Nov 2017	Backscatter	Edgetech 4200 SSS 300 kHz: **H2:** HSM LF, 150 m range, cable out = 11–27 m **H5:** HSM LF 150 m range, cable out = 40 m
		Bathymetry	Kongsberg EM710 MBES: Transmit mode: Very Shallow Frequency range: CW 65–105 kHz Pulse length [msec]: 0.2 Swath width = 90°
HE 505	13–20 Mar 2018	Backscatter	Edgetech 4200 SSS 300 kHz, **H2:** HSM LF 150 m range, cable out = 25 m **H3:** HSM LF 70 m range cable out = 30–40 m **H5**: HSM LF 150 m range, cable out = 61 m
		Bathymetry	Kongsberg EM710 MBES: Transmit mode: Very Shallow Frequency range: CW 65–105 kHz Pulse length [msec]: 0.2 Swath width = 90 °

and (3) to determine changes using the Digital Shoreline Analysis System (DSAS v.5), a plug-in tool in ArcGIS (from version 10.4 onwards) developed by the United States Geological Survey (USGS).

2. Study area

Our study was conducted within the Special Area of Conservation (SAC) site "Sylt Outer Reef" in the German Bight, North Sea (Fig. 1). A high-resolution area-wide SSS mosaic was acquired in the western part of the SAC in 2013 by (Papenmeier et al., 2018), a portion of this survey is shown in Fig. 1. The SSS mosaic combined with adequate ground-truth information was the basis for a high-resolution sediment distribution map (BSH, 2018; Papenmeier et al., 2018). The sediment classes range from muddy sand along the edge of the Paleo Elbe Valley (PEV) (Fig. 1), to patchily distributed Holocene sands and coarse-grained lag deposits (fine gravel and larger, including cobbles and boulders). We used these data set to select three focus areas (H2, H3, H5, Fig. 1) located in the Sylt Outer Reef. Here, sharp as well as gradual shifts between coarse and finer sediments exist. The focus areas differ in their complexity of sediment and boundary patterns.

Area H2 (10.3 km^2) is the least complex area with only one sharp sediment boundary between high and low backscatter intensities, followed by a gradual backscatter decrease (Fig. 4). H3 is the largest (12.8 km^2) and most complex area (Fig. 5). The boundary between high and low backscatter intensity is strongly sinuous. Gradual changes are less present. Area H5 (2.5 km^2) shows similar backscatter features with H2 (sharp boundary with following gradual change), but the sharp boundary in H5 is curvier than in H2 (Fig. 6).

2.1. Hydrodynamics in the German Bight

The heterogeneous sediment patterns being present at the Sylt Outer Reef are assumed to be formed by hydrodynamic forces (Diesing et al., 2006; Staneva et al., 2009; Zeiler et al., 2000).

In general, depth-average circulation in the shallow part of the German Bight can be characterized as counter-clockwise (e.g. Callies et al., 2017; Port et al., 2011). The depth-averaged currents are directed along the coast, which result in cyclonic circulation in the German Bight due to its topography. The reason is that the typical south-western wind pattern enhances the tidal residual circulation in the direction of propagation of the Kelvin tidal wave. However, despite a typical pattern, wind magnitude and direction can vary greatly both in short- and long-term perspectives, having a pronounced and complex response on the circulation. The tidal range in the coastal areas of the German Bight varies from ~1.5 to 3.6 m with a dominance of the semi-diurnal tidal constituents (Androsov et al., 2019; Fofonova et al., 2019; Maßmann et al., 2010; Plüß, 2003). The average significant wind-induced wave height is 1–1.5 m and driven mainly by westerly and southwesterly winds (Quante and Colijin, 2016). Storm events approaching from the northwest and southwest directions can induce water levels up to 5 m above mean sea level, for the duration of one or two tidal cycles (Zeiler et al., 2008). During some extreme storm events, maximum wave heights have exceeded more than 5 m (Fenoglio-Marc et al., 2015; Leiding et al., 2013). Tidal residual circulation and asymmetry patterns, wave actions, and wind-driven flows interacting through a number of mechanisms (e.g., Soulsby et al., 1993) determine the sea bed dynamics. Their mutual feedback has pronounced non-linear character in the coastal zones (e.g., Staneva et al., 2016). Strong currents in response to extreme events and storm tides significantly modify the coastal sea bed morphology, where the bed-forms peculiarities are largely defined by the resulting wavelength spectrum (Armonies et al., 2014; Clukey et al., 1985; Korevaar, 1990; Michaelis et al., 2019a; Otto et al., 1990).

3. Data and methods

Primary hydroacoustic data sets (SSS and MBES) acquired over the three study areas were used in this study. The overall methodological workflow is presented in Fig. 2. The initial task was to generate a Digital Terrain Model (DTM) and Dynamic Surface from the MBES data, which were used afterwards to georeference the SSS data. Subsequently, SSS data were processed to eliminate geometric and radiometric artefacts, and to improve positional accuracy. Lastly, the mosaics were classified to extract the sediment boundaries of the lag deposits, which were then analyzed for positional change through time.

3.1. Data acquisition

Hydroacoustic data presented in this study were obtained from surveys performed in 2016, 2017, and 2018 (Table 1) in the focus areas (Fig. 1). The 2016 survey was only conducted in H3, while only H2 and H5 were visited in 2017. All focus areas were surveyed in 2018. All surveys were conducted with the German research vessel "Heincke".

SSS backscatter data were acquired with an Edgetech 4200 MP SSS with a frequency of 300 kHz (double pulse mode) towed at a speed of 5 kn, and at an altitude of 15% of the average depth of the survey area. The SSS was towed behind the ship with varying length of cable out, because the water depth fluctuated in each focus area during the surveys (Table 1). Surveys were designed to achieve a 10% overlap and 0.25 m along-track resolution for the SSS mosaics. The SSS settings were controlled on-board with the Edgetech Discover Software. Survey settings for each study area are indicated in Table 1.

The Kongsberg EM710 MBES was simultaneously deployed, but the track distances were too wide to achieve a swath overlap. The EM 710 may be set in different transmit modes depending on the depth ranges in the survey area. The very shallow mode, which is ideal for < 100 m depth range, was used in our surveys. The frequency range used in this mode was 65–106 kHz and the pulse length was 0.2 msec. The maximum reliable swath width was 90°.

The MBES was fixed mounted in the hull and connected to Trimble SP461 DGPS receiver (DGPS mode horizontal accuracy:

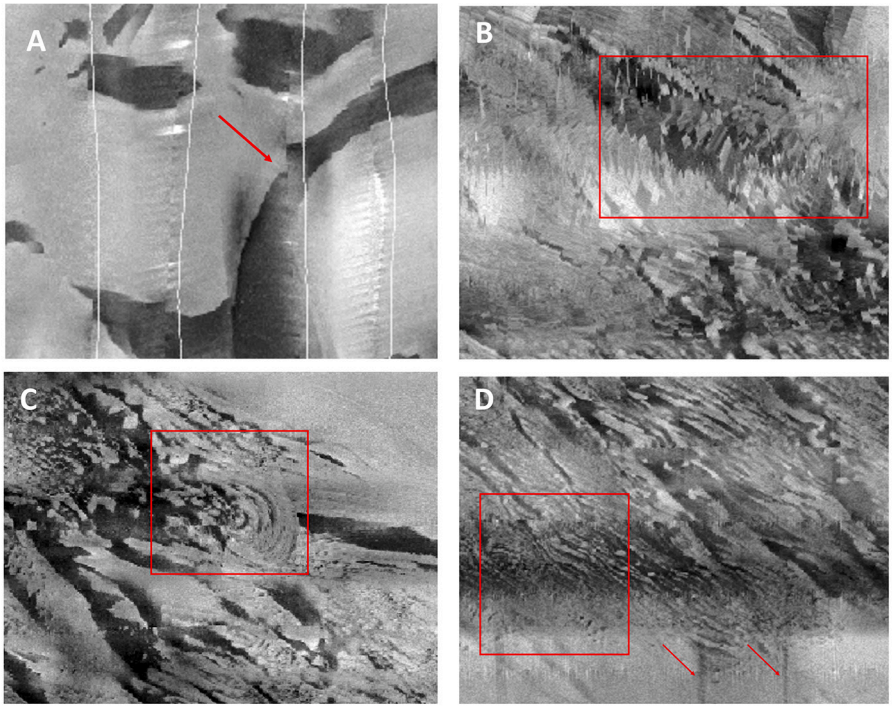

Fig. 3. (a) Offset in the nadir as a result of missing altitude data in the SSS files (b) Slices artefact (c) Swirls artefact (d) seam artefact or poor line blending that were caused by insufficient swath overlap and changed in cable out of the towed SSS during the survey.

0.25 m + 1 ppm RMS) (Trimble, 2019). Heading, roll, pitch, and heave information were recorded by an Ixsea PHINS III Inertial Navigation System (INS). The settings of the MBES were controlled with the SIS-Kongsberg Acquisition software.

3.2. Data post-processing

3.2.1. Processing of MBES data

Initially, MBES data were processed to create a DTM and Dynamic Surface, which were necessary to process SSS data. Post-processing was carried out in QPS Qimera v 2.0.1 software to correct the raw MBES data from tidal effects and reject invalid soundings. Tidal effects were removed from the raw data using the inverse tidal solution (Egbert and Erofeeva, 2002), because the study area is far from tide gauges and the installation of temporary gauges was not possible during the surveys. In particular, the tidal correction was made based on TPXO9-atlas. It is obtained by combining 1/6-degree base global solution TPXO9.v1 and thirty 1/30-degree resolution local solutions for all coastal areas, including North Sea. Various altimetric (Topex Poseidon, Topex Tandem, ERS, GFO) and other data sets (i.e. tide gauges, ship born ADCP) were assimilated into it. The RMS misfit for the major tidal component M2 is less than 2.79 cm and the root-sum-square of the RMSs for major 8 harmonics is less than 4 cm for the European Shelf (TPXO9; (Egbert and Erofeeva, 2002; Stammer et al., 2014)).Corrected bathymetry data were produced and exported as gridded bathymetry (ASCII format) at 1-m grid resolution. Subsequently, the ASCII bathymetric data were transferred to ArcGIS (v.10.7.1) for interpolation. The Topo-to-Raster interpolation function was used to interpolate the gaps in the bathymetric data. The interpolation produced DTM surfaces in TIFF format with 1 m cell size. The DTMs were integrated in the QPS Fledermaus Geocoder Toolbox (FMGT) to georeference the SSS data.

3.2.2. Processing of SSS data

The SSS backscatter data were processed in QPS FMGT v.7.8.8 software. The software applied backscatter corrections, beam pattern corrections, and angle-varying gain (AVG) corrections to the raw SSS backscatter. After these adjustments, georeferencing of each survey line was conducted by importing a reference grid (DTM) and navigation files into FMGT. The software georeferenced and corrected the SSS time series from slant range using the bathymetric model, beam pattern compensation, speckle noise removal, overlap and feathering options to create a more visually consistent mosaic (Fakiris et al., 2018). The DTM was also utilized to improve the SSS pixel georegistration (Quality Positioning Services, 2018). Additionally, FMGT applied the sonar's attitude (i.e. XY coordinates, roll, pitch, heave) using the navigation files to improve the spatial accuracy of the SSS data. In some instances, adding navigation data automatically adjusted the layback offset. However, during our experiments we noticed that despite adding a reference grid and navigation data, manual layback adjustments were still needed to locate the actual position of each snippet.

Manual layback correction was done by using the MBES backscatter and DTM as a reference behind the SSS mosaic. The SSS mosaic's transparency was adjusted to see the DTM/MBES mosaic in the background, and the offset was measured with the 'measure tool' of FMGT. The offset value was then entered in the 'Apply Layback' option of the processing settings in FMGT.

Finally, side-scan snippets were mosaiced with the 'No Nadir possible, 25% overlap' algorithm to reduce the banding effect, and 50% line blending was applied to blend the pixels in the overlapping areas. The SSS mosaics were gridded to 0.25 m resolution with dB values cropped to ± 3σ and logarithmically mapped to 8-bit scale. Final mosaics were exported in 'Colored GeoTIFF (georeferenced TIFF)' format with three RGB bands. A step-by-step guide on how to process SSS data in FMGT is provided as supplementary material.

3.2.3. Issues encountered with FMGT

We encountered some problems when we processed our SSS data in FMGT. First, we lost the altitude information in our SSS data after we converted our original files from JSF to XTF. The conversion was necessary because JSF files are incompatible with FMGT. As a result, the lack of altitude information caused an offset in the nadir during the bottom tracking process (Fig. 3A). This issue was addressed by QPS

when we reported it. They released a new version of FMGT (v.7.8.8), where they added an option to adjust the energy threshold for bottom detection. The 'Compute Bottom Detection' function in FMGT uses a bottom detection algorithm to compute the altitude value for use in FMGT. The energy threshold value is a cumulative energy threshold that uses the sum of the energy returned from the seafloor to determine the minimum slant range (Quality Positioning Services QPS, 2018). To lessen the offset in the nadir, the Energy Threshold value must be set as low as possible (e.g. 1%). However, this solution did not completely remove the nadir offset in some of our SSS data (Fig. 3A). Therefore, areas with nadir offset were not traced as part of the boundary and were excluded in the change analyses.

Another problem that we encountered are 'swirls' and 'slices' artefacts in the mosaic (Fig. 3B and C). These were observed when the 'Navigation Parameters' options were activated in the Settings Menu. We fixed the 'swirls' artefacts when we deactivated the 'Apply Layback' and 'Course Made Good' options, and increased the 'Heading Spline Smoothing' value. The 'slices' artefacts were solved when we added navigation files from the SSS, turned off the apply layback, activated course made good, and increased the heading spline smoothing value.

Moreover, we observed poor line blending of the snippets or seam artefacts (Fig. 3D). Some snippets appear darker than others. A personal communication with the software developers revealed that these artefacts were caused by insufficient overlap between the lines, which makes it difficult to compensate the outer beams. We also noticed that this artefact appeared in areas where we changed the length of cable out when towing the SSS during survey. The seam artefacts were fixed by increasing the 'Angle Varying Gain' (AVG) values in the settings menu.

3.3. Data analysis

Side-scan mosaics were transferred to ArcMap v.10.7.1 for backscatter boundary extraction, baseline construction, and boundary change calculation (Fig. 2). The first two stages in the data analysis were the data preparation for the DSAS v.5. The software can be downloaded for free at https://www.usgs.gov/software/digital-shoreline-analysis-system (United States Geological Survey, 2019). DSAS calculates changes in shoreline positions and provides a robust quantification of the movement (Himmelstoss et al., 2018). The tool has been used globally to determine shoreline migration, coastal change, and coastal dynamics (Burningham and French, 2017; Del Río et al., 2013; Komar, 2010; Oyedotun, 2014).

3.3.1. Boundary extraction

Required data for DSAS are shorelines (backscatter boundary lines in our case) from different years, baselines, and transects. In this study, boundaries were extracted from SSS mosaics collected in 2016, 2017 and 2018 over the focus areas (Figs. 4, 5, and 6).

Firstly, SSS mosaics were transferred to ArcMap (v.10.7.1) and were classified based on pixel values to differentiate lag deposits from finer sediments. Backscatter values ranged from 0 to 255 in the 8-bit raster image. Mosaics were classified into two classes with the 'Reclassify' tool of ArcMap using the Natural Breaks (Jenks) Classification method. Jenks is an unsupervised data classification method that divides data into classes based on natural groupings inherent in the data. The method was proven to have the ability to distinguish between similar-looking features (Montereale Gavazzi et al., 2016). Lag deposits corresponded to higher backscatter (darker colors in our scale: grayscale values 55–255), while the surrounding finer sediments corresponded to lower backscatter (lighter colors in our scale: grayscale values (0–54)) (Figs. 4, 5, and 6).

Secondly, the classified raster images were converted into polygons to extract the boundaries of the lag deposits. Subsequently, polygons were converted into lines because DSAS requires feature lines as input.

The boundary lines must be formatted with the appropriate attributes for use within DSAS. Required user-defined field attributes are the date and uncertainty of each shoreline (boundary line) (Himmelstoss et al., 2018). The uncertainty field in the attribute table accounts for the positional uncertainty of each shoreline/boundary, which DSAS will consider in the calculation of change statistics. The calculated rates of change provided by DSAS can only be as reliable as the measurement and sampling errors accounted for when compiling each shoreline position. The uncertainty value is defined by the user, and is calculated by accounting both positional uncertainties associated with natural influences and measurement uncertainties (i.e. digitization or global-positioning-system errors) (Himmelstoss et al., 2018). We assigned an uncertainty of ± 0.5 m to each boundary line. This was calculated as the sum of the SSS mosaic's grid resolution (0.25 m) and the horizontal accuracy of the DGPS used for MBES during the survey (0.25 m + 1 ppm RMS) (Trimble, 2019). We considered the accuracy of the DGPS because we used the MBES data to georeference the SSS mosaics. Moreover, the overall uncertainty of the change calculation results is ± 1 m, which is the sum of the uncertainties of the two boundary lines that were measured.

Lastly, all shorelines were required to be merged as one feature class and be in meter units in a projected coordinate system (Himmelstoss et al., 2018). Boundaries were merged to a single file and projected to Universal Transverse Mercator (UTM) Zone 32N-WGS 84 datum. Boundary lines for each study areas are shown in Figs. 4, 5, and 6.

3.3.2. Baseline construction

DSAS uses a measurement baseline method to calculate rate-of-change statistics for a time series of shorelines (Leatherman and Clow, 1983). The baseline in DSAS is constructed by the user and serves as the starting point for all transects cast by the application (Himmelstoss et al., 2018). Transects are evenly-distributed lines perpendicular to the baseline that intersect each shoreline (here: sediment boundary line) to create a measurement point, and these points were used to calculate shoreline/boundary line change rates.

Baselines can be created by buffering an existing shoreline/boundary line or by creating a new feature class and manually draw the baseline. The baseline can be constructed at the left, right or both sides of the boundary lines. For this study, baselines were drawn manually because it was the most efficient approach given the complex structure of the sediment boundaries in the study areas (Figs. 4, 5, and 6). DSAS requires that the proper baseline flow orientation be defined to ensure that rates of change are expressed correctly as negative and positive values (Himmelstoss et al., 2018). In this regard, baseline segments were placed to the right of the boundaries if they showed a 'positive trend' or to the left if they showed a 'negative trend' (see Section 3.3.3). Finally, baselines were projected to a common coordinate system in meter units (UTM Zone 32 N-WGS 84) containing the attribute fields required by DSAS (i.e. ID, Group, and search distance).

3.3.3. Boundary change analysis in DSAS

To determine the trend of boundary movement, we used the boundary of the first survey as reference to define the change direction. Consequently, it was defined as a positive trend or 'boundary advance' if the boundary line of the new survey moved to the right of the boundary of the first survey. Negative trend or 'boundary retreat' is when the newest boundary (from recent survey) moved to the left of the boundary of the first survey. For example, it was considered as boundary retreat if the sediment boundary from 2017 moved backwards of the 2018 boundary.

Before running the DSAS tool all boundary lines and baselines must be stored in a personal Geodatabase as feature lines with the required attribute fields.

The workflow for running the DSAS toolbar is shown in Fig. 2. The first step is to define the default parameters in the 'Set Default Parameters' window such as selecting the attribute field of the date of the boundaries, uncertainty values, and baseline ID.

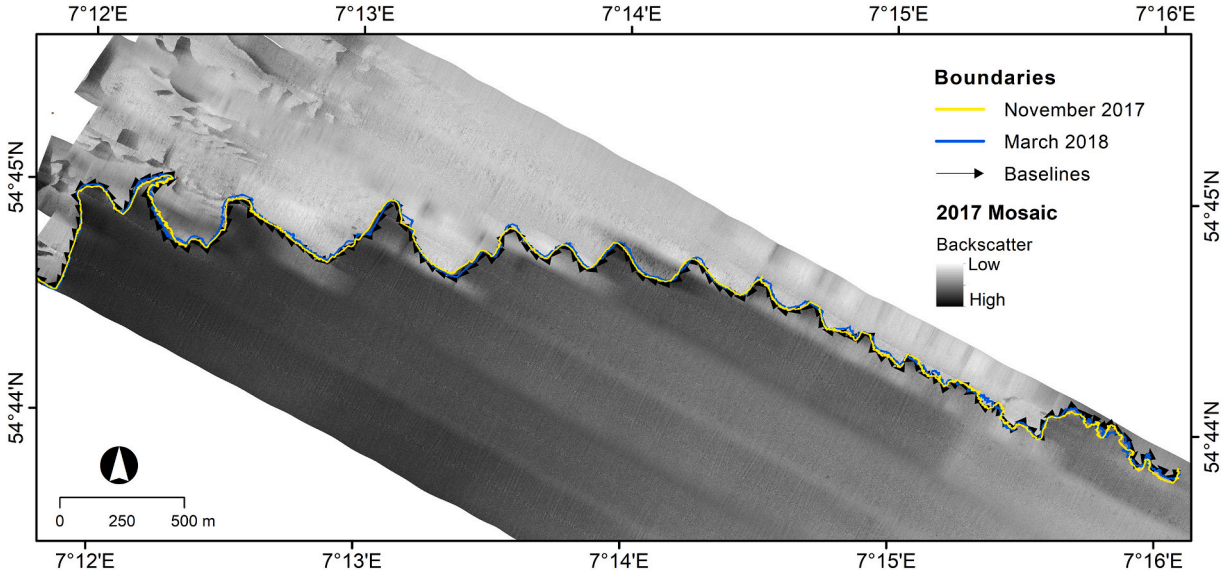

Fig. 4. Sediment boundaries of in H2 and the orientation of the baselines as indicated by the arrows. DSAS uses a measurement baseline method to calculate rate-of-change statistics for a time series of shorelines/boundaries.

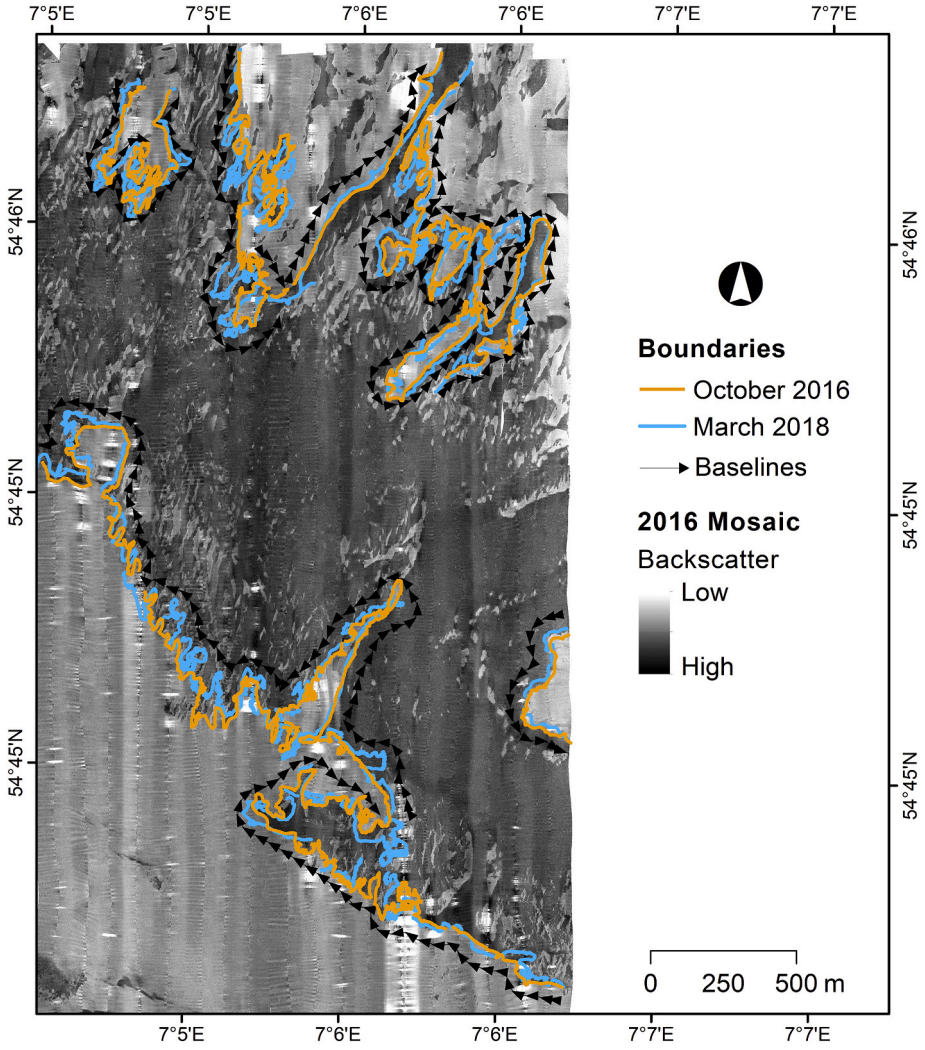

Fig. 5. Investigated sediment boundaries of the lag deposit in H3. Arrows indicate the orientation of the baselines.

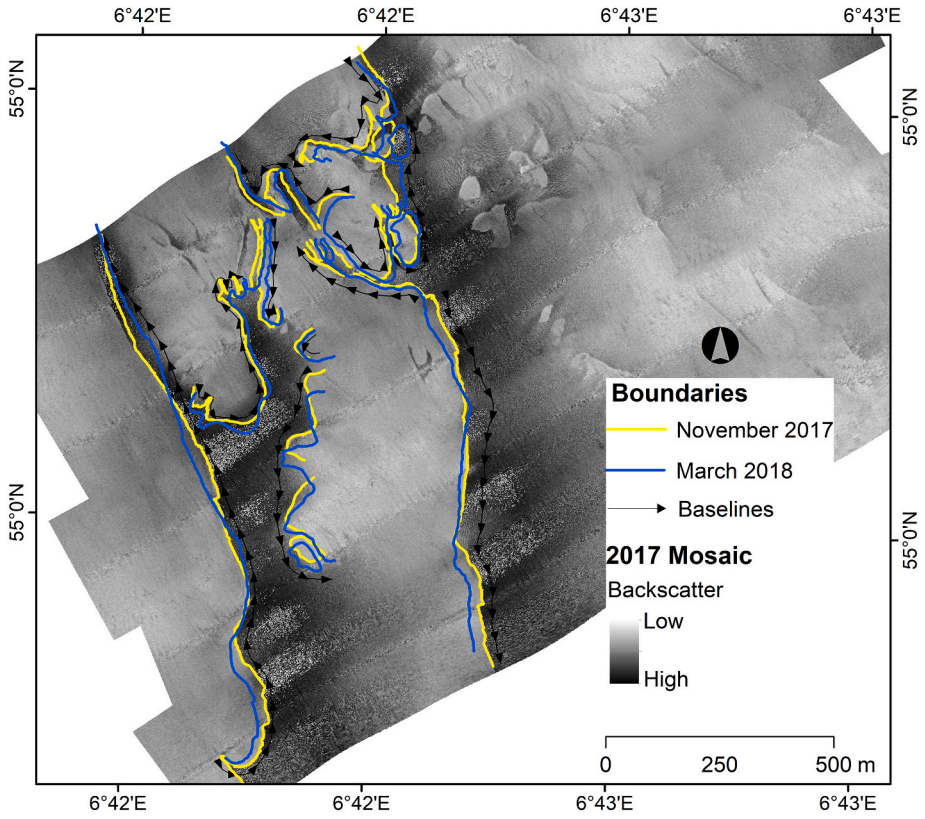

Fig. 6. Sediment boundaries of the two-parallel lag bedforms and the position of baselines in H5. Arrows indicate the orientation of the baselines.

Secondly, transects must be cast based on user-specified transect spacing. Transects were cast at 5-m interval in every focus area. The program generated 1497 transects for H2, 2586 transects for H3, and 1058 transects for H5. Transects were manually edited in ArcMap to ensure that each transect line intersects all boundary lines.

Finally, DSAS offers different statistical analyses including the Net Shoreline Movement (NSM), which reports the distance between the oldest and youngest shorelines (Thieler et al., 2017). NSM was calculated for all study areas, but is referred in this paper as Net Boundary Movement (NBM). Other statistics in DSAS require more than two shoreline data sets, hence they were not performed in our analysis. Detailed guidelines on how to use DSAS are found in the DSAS v5.0 User Guide by Himmelstoss et al. (2018).

4. Results

4.1. Improvement in SSS mosaics

Towed SSS can cause dislocations and distortions in the resulting image. To correct these, our data were processed using the FMGT software. Our results showed an improvement in the visual quality of the SSS mosaics in terms of backscatter contrast, reduction of artefacts, stitching of SSS strips, and layback correction.

Backscatter intensity were normalized throughout the mosaics (Fig. 7B and D). The dark-line artefacts caused by the change in layback during the survey were removed (Fig. 7A and C). The result was noticeable in the northwestern corner of the H2 mosaic. However, some of these artefacts can still be seen as an abrupt change in grey contrast as observed in the 2018 mosaic of H2 (Fig. 7D). In addition, the nadir artefacts in H3 were fixed except in some areas in the southern part of the mosaics (Fig. 8B and D). The lag deposit features were also clearer and traceable compared to the raw H3 mosaics (Fig. 8A and C).

Lastly, dislocations of the SSS strips were corrected by the geo-referencing method (Fig. 9). The red line was the location of the boundary in the SSS mosaic of H3 before geo-referencing. The blue line was the georeferenced location of the boundary. The background mosaic is the backscatter data from MBES that was taken at the same time with the SSS data. We measured a difference of approximately 47 m between the non-geo-referenced boundary and georeferenced boundary. Improvement in the alignment was observed in the processed mosaics of H5 (Fig. 10B and D).

4.2. Description of the focus areas

Focus Area H2 with the less complex sediment and boundary pattern has a single sharp, sinusoidal boundary that stretches from west-northwest to east-southeast. Low backscatter intensity (fine sand) was observed at the north of the boundary. South of the boundary of H2, a decreasing backscatter intensity from west-northwest to east-southeast was observed (Fig. 11). Based on this change in backscatter intensity, we inferred that the sediments gradually changed from fine gravel to fine sand at the boundary. H2 is situated in relatively shallow areas of the SOR in comparison to the other focus areas, with depth ranging from 22 to 27 m. Depth increases from the southeast towards the boundary line in the northwest (Fig. 11). The boundary was found in the deeper part of H2 (~27 m).

The mosaics of H5 revealed two patches that are parallel to each other with a north-south orientation (Fig. 12). Both features have sharp boundaries in the western edge and gradual boundaries towards the east. The bathymetric model showed that the two deposits were located in different depths, which separates them from each other. The boundaries were situated in the deeper areas (40–42 m), while the gradual boundaries were located in shallower flanks. H5 is located in the deeper area of the SOR compared to the other focus areas, where depth ranges from 36 to 42 m. High backscatter areas are situated along the slope where the bathymetry decreased, while the low backscatter regions are situated in higher elevation.

The largest focus area H3 is characterized by one large elongated,

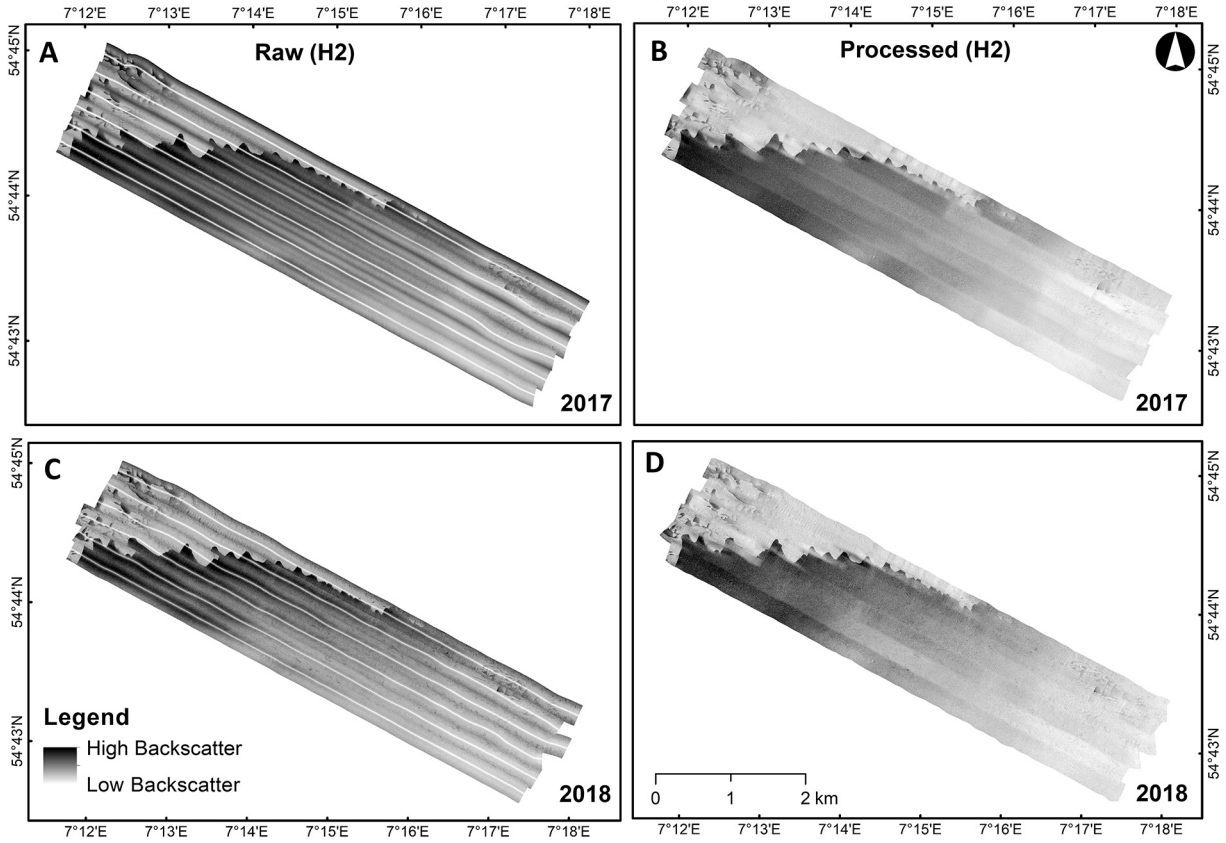

Fig. 7. Backscatter intensity were normalized in the H2 mosaics. Dark-line artefacts can be seen in the raw image (left). After processing, the artefacts were lessened but they are replaced by an abrupt change in grey contrast in some part of the processed mosaics (right).

high backscatter feature oriented towards northwest-southeast direction (Fig. 13). Smaller patches of low backscatter intersect the large features. Boundaries are mostly sharp but gradual boundaries are present in the southwest of the feature. From studies by Papenmeier and Hass (2018), it is known that high backscatter of the large feature is differing to H2 and H5. Here, lag deposits including boulders are present. The small high backscatter patches north of the main feature have comparable sedimentology as H2 and H5. The bathymetric model revealed that the boundaries were located in the depressed areas of H3 (~36 m), while areas with lower backscatter were in relatively shallow bathymetry (~28–30 m) (Fig. 13).

4.3. Changes in boundary position

The analysis of change using the DSAS method was conducted to observe if changes in the position of the boundaries exist. Our results (Figs. 14, 15, and 16) showed an interesting common trend in the movement of the boundaries. In general, we noticed that the boundaries moved from northeast to southwest direction in every focus area. Boundary movements of less than 20 m were usually observed (Fig. 17). Boundary retreat was dominant in H3 and H5, while boundary advance prevailed in H2.

H2. The trend of movement in H2 is towards the NE-SW direction (Fig. 14). Of the 1497 transects, 66.5% have measured boundary advances and 33.5% recorded boundary retreats (Table 2). The maximum boundary advance was 36.5 m, while the maximum boundary retreat was −35.6 m. We observed that the most common movement was boundary advance of < 10 m (Fig. 17).

H3. Boundary movements are more complex in H3 (Fig. 15). The boundaries are moving towards the center of the investigated feature. The northeastern boundaries moved to the SW direction, while the southwestern boundaries moved towards northeast. Boundary retreats are mostly observed in H3 (59% of 2586 transects) and the maximum distance recorded was −183.5 m (Table 2). The majority of the transects recorded boundary retreats of −1 to −20 m (Fig. 17). Movements of > 40 m, both advance and retreat, were observed in the southwestern boundary.

H5. The direction of boundary movement in H5 was from northeast to southwest (Fig. 16). Approximately 54.3% of the 1058 transects have measured boundary retreats (Table 2). The maximum distance was −47.9 m. Boundary advances were measured by 59.3% of the transects and were mainly observed from the center to the south of H5. The maximum advance distance was 88.5 m. The most frequent movement in H5 were boundary retreats of less than 1 m (Fig. 17).

5. Discussion

Comprehensive monitoring of marine sedimentary ecosystems has been recommended to quantify large-scale and cumulative effects of anthropogenic impacts, and to protect the sedimentary ecosystem (Heery et al., 2017). Our methods for detecting sediment shifts using SSS data can be used for large-scale and long-term environmental monitoring programs (years or decades), to help us understand and locate the effects of sedimentological changes to benthic habitats and marine ecosystem services (Thistle et al., 1985; Troell et al., 2005). Our findings suggest that SSS was effective to detect changes in the boundary of submarine sediment facies following the processing as described in this paper. By producing comparable mosaics with improved spatial accuracy, we were able to classify them and perform change detection. The DSAS method was able to quantify the change in boundary position and provided information on the trends of movement. However, it is also important to note that variations in seafloor

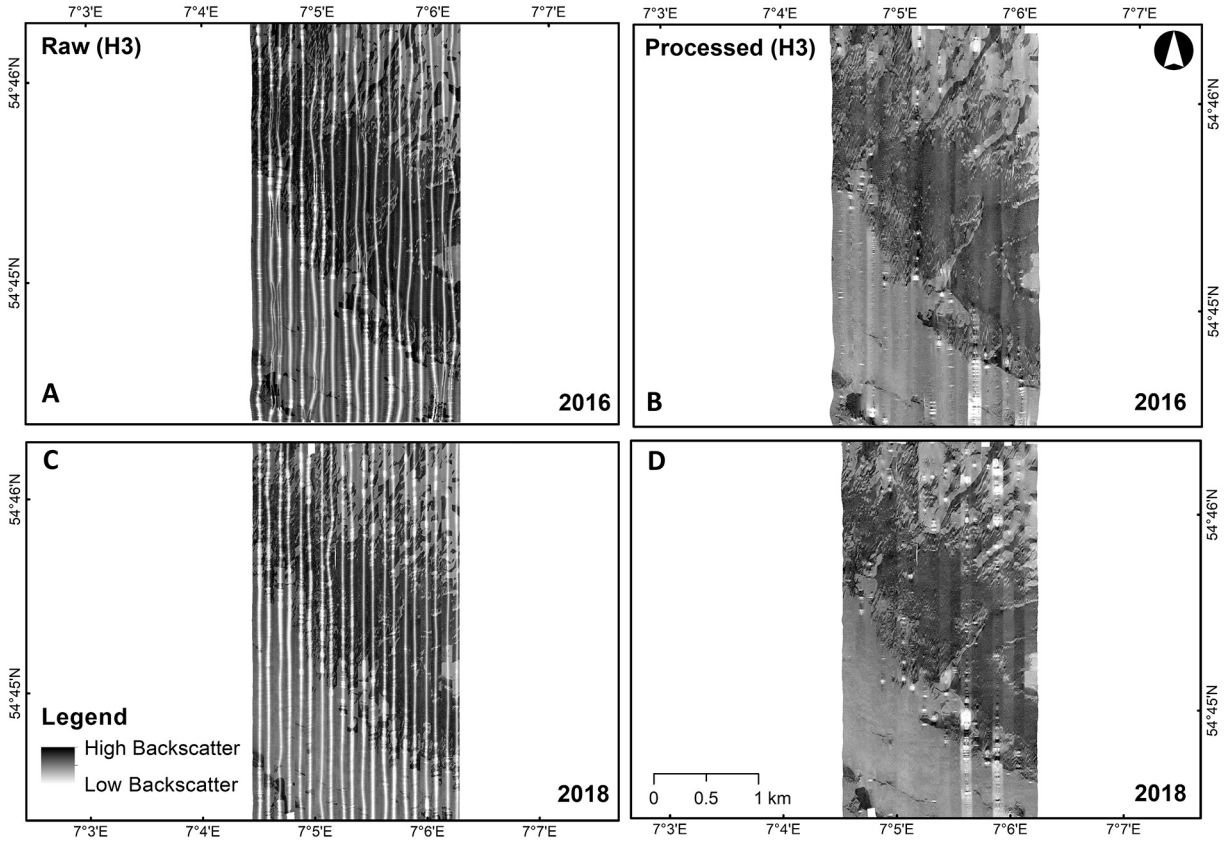

Fig. 8. Nadir artefacts were observed in the raw mosaics of H3, which makes the lag deposit difficult to be seen (left). The artefacts were lessened in the processed mosaics but some were still visible in the southern part.

sediment type may be caused by multiple sources of environmental factors that influence the backscatter measurements during surveys. A recent study of Montereale-Gavazzi et al. (2019) highlighted the importance of short-term environmental dynamics on the interpretation of observed changes derived from time-series MBES backscatter data. The authors found that short-term tidal variability may affect the

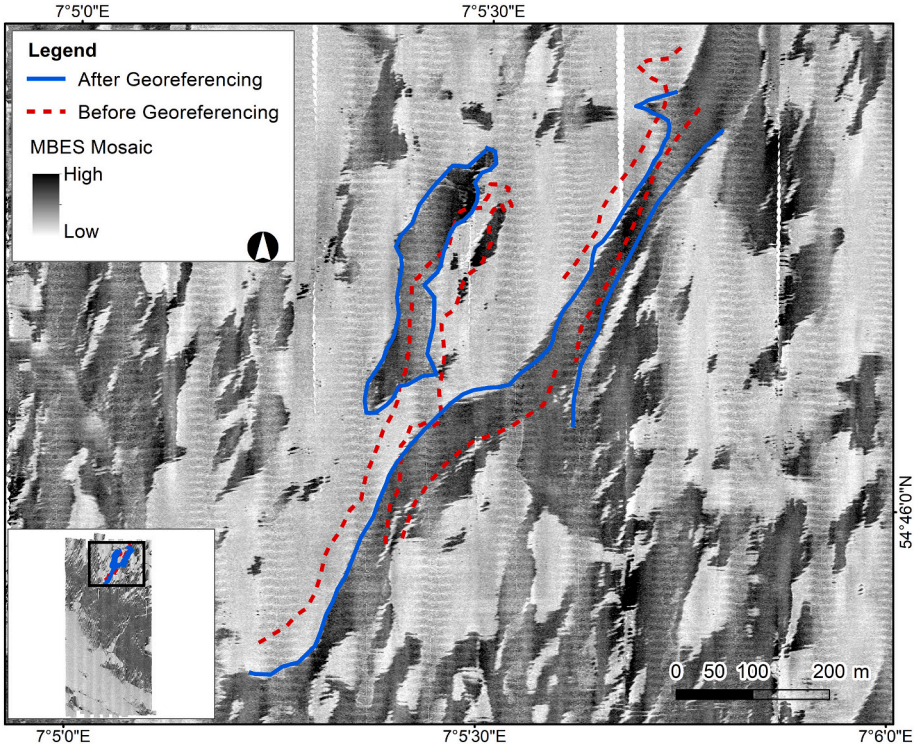

Fig. 9. Improvement in the spatial accuracy of the SSS mosaic is represented by the blue line in this image. The blue line was the traced boundary after we georeferenced the SSS data using the MBES data. The red line shows the location of the boundary before georeferencing. By measuring one point in this image, we saw a difference of around 47 m between the pre-georeferenced line and georeferenced line. The basemap is the backscatter mosaic from MBES. (For interpretation of the references to color in this figure legend, the reader is referred to the web version of this article.)

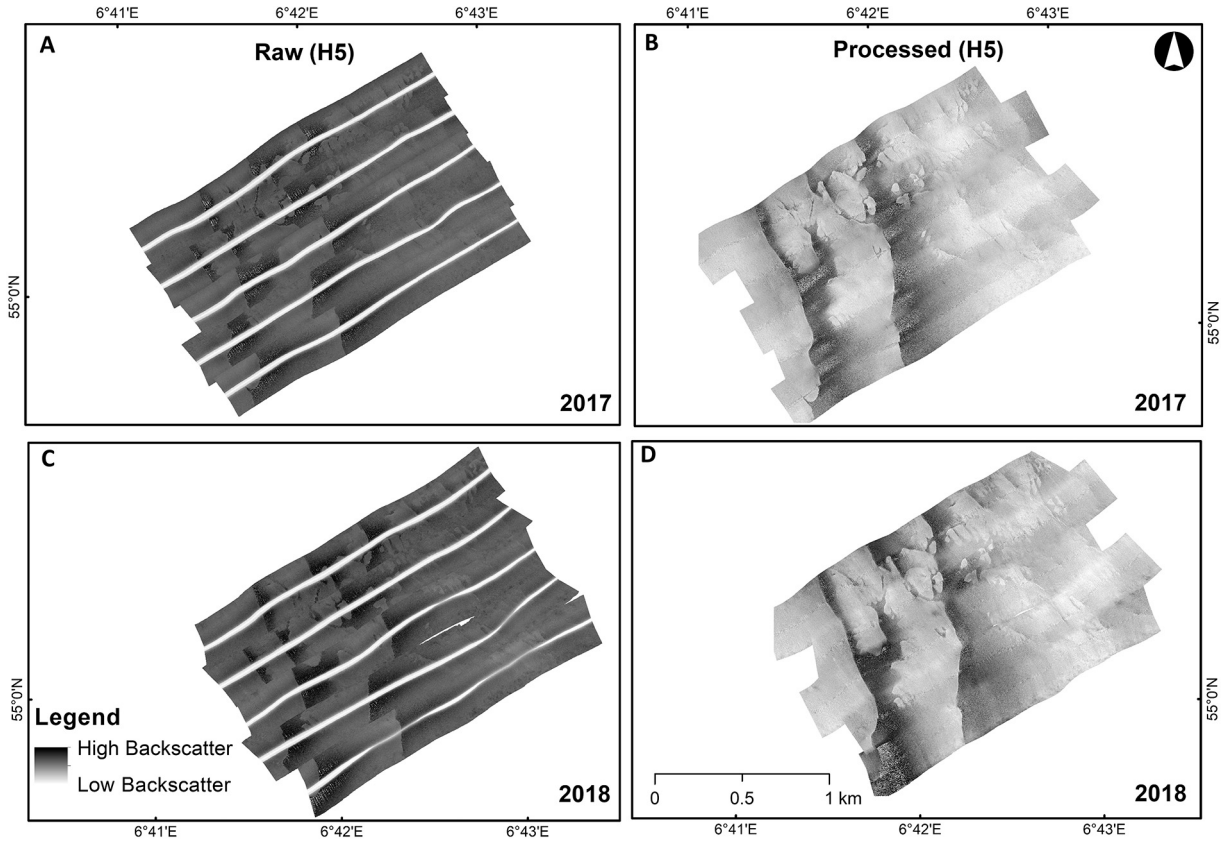

Fig. 10. The layback offset was visible in the raw mosaics of H5 (left). After georeferencing, the SSS strips were aligned properly and the lag deposits became more visible (right).

backscatter field measurements, and may consequently influence the detection of actual changes on the seabed.

All of the methods that we presented were semi-automated, repeatable and were readily available in off-the-shelf software namely ArcMap, QPS Qimera, and Fledermaus Geocoder. We have tested the capacity of FMGT to process SSS data and showed that data from MBES can be used to correct the layback offset. This is especially relevant when working in shallow water, where time and budget constraints might prevent full coverage surveys with MBES. Using MBES data to correct geometric artefacts on SSS images have been conducted before (Cervenka et al., 1994), but our approach is easier to implement.

The results exhibited improvements in the quality of the SSS mosaics, especially on the backscatter-level normalization and layback correction. The improved spatial accuracy of our SSS mosaics

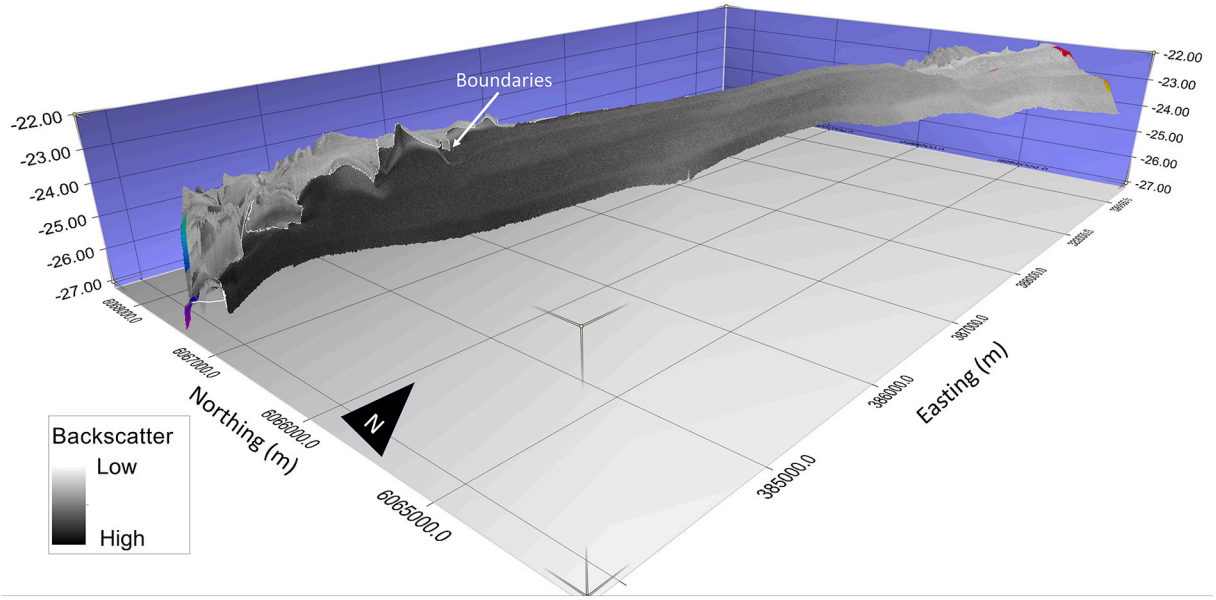

Fig. 11. Mosaic of H2 in 2017 and draped over the bathymetric model of the same year (high backscatter = dark colors) The sediment boundary of H2 is a single sinuous line that stretches from west-northwest to east-southeast. The depth range is 22–27 m.

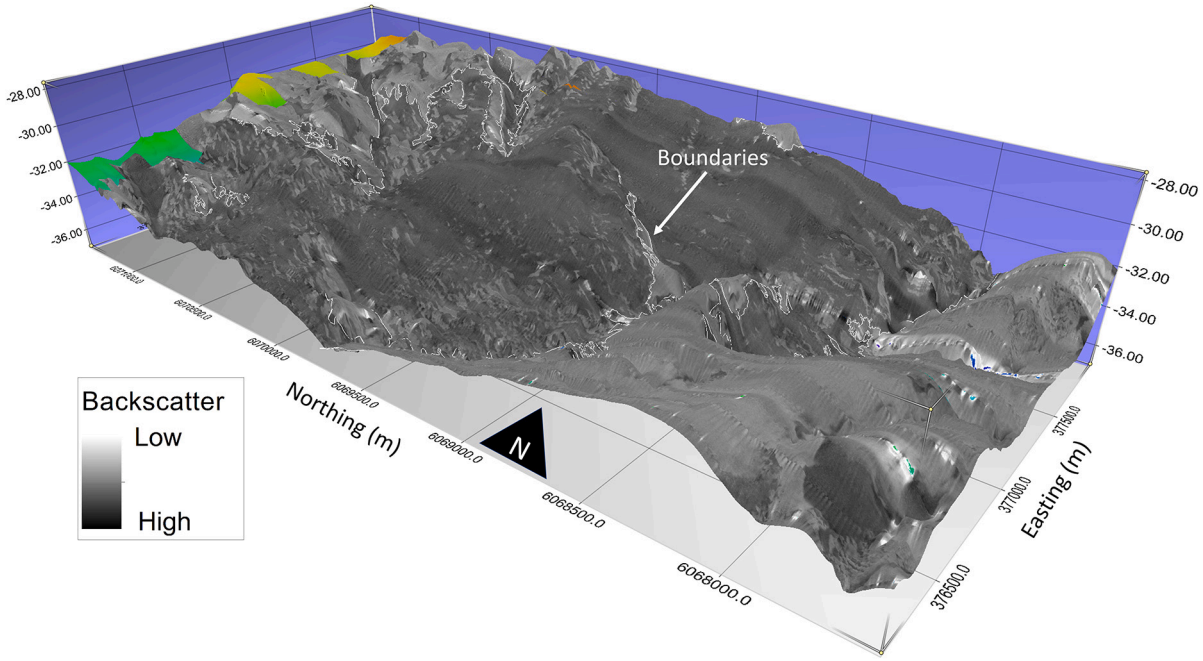

Fig. 12. The 2017 SSS mosaic of H5 showing the two parallel sharp boundaries of the coarse sediment (high backscatter = dark color) deposits on one side and gradual boundaries on the other. The 2017 mosaic overlaid in the bathymetric model of the same year. The bathymetry of H5 is decreasing from northeast to southwest and the boundaries were found in areas with lowest bathymetry [40–42 m].

(± 0.25 m) was better than the accuracy of the SSS mosaics that were previously reported, where their spatial accuracy was ± 25 m (Diesing et al., 2006) or not even specified (Mielck et al., 2015). This accuracy is necessary when small-scale changes related to storm or tidal events are in the focus of the investigation.

DSAS is useful for addressing features, which can be presented as lines at a particular point in time (Oyedotun, 2014). It has been used to quantify long-term changes in sediment dynamics in the coastal areas (Aedla et al., 2015; Bera and Maiti, 2019; Komar, 2010), but not yet in submarine features. Our findings suggest that DSAS can quantify changes of not only shorelines, but also submarine features such as sorted bedforms or lag deposits. In contrast to other methodology presented before (Diesing et al., 2006; Mielck et al., 2015), our method was able to provide a more detailed quantification of the variability of sorted bedform boundaries. Moreover, if additional data sets will be collected over the focus areas, we might be able to provide information on the sediment dynamics for longer timescales and to project possible changes. DSAS v5.0 can calculate shoreline forecast (10–20 years into the future) based on historical shoreline position data, but this requires a minimum of four shoreline positions as input data (Himmelstoss et al., 2018). Whether such forecasts of sediment boundary movement are reliable, would be interesting to investigate but does require additional repeat surveys. Furthermore, the ability to input uncertainty values in DSAS, as mentioned in Section 3.3.1., enhanced the reliability of the

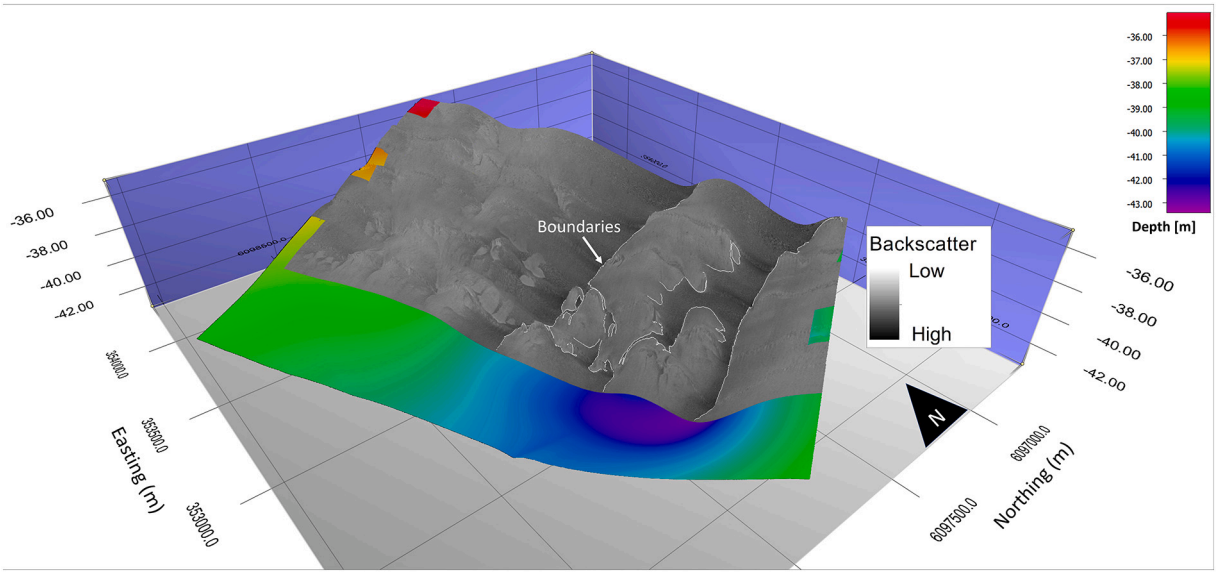

Fig. 13. Mosaics of H3 from the 2016 survey. Sharp boundary lines with northeast-southwest orientation separate the coarse sediments (high backscatter = dark color) from the surrounding finer materials (low backscatter). The 2016 mosaic overlaid in the bathymetric model of the same year shows that the boundaries were located in deeper areas.

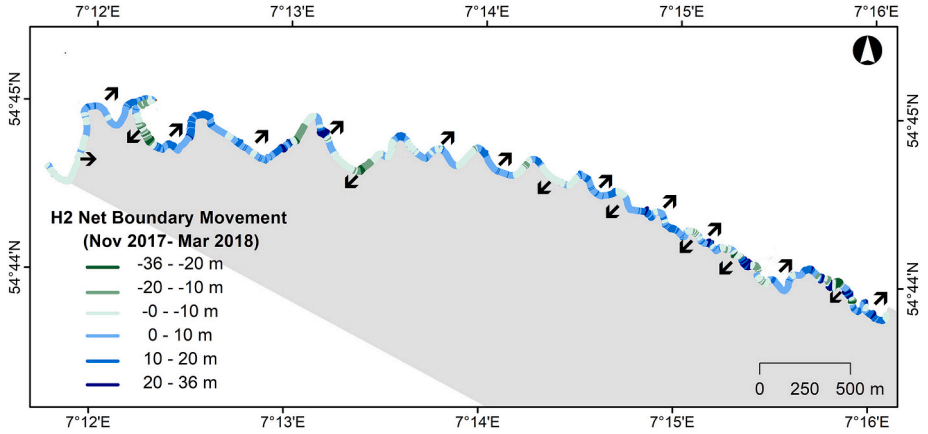

Fig. 14. Net boundary movement in H2 within four months. The direction of movement was observed to be from northeast to southwest.

results.

5.1. Changes in sediment boundaries and underlying factors

The observed changes in the sediment boundary position indicate sediment shifts, or change from coarser sediment to finer sediments. The range of boundary movements (1–184 m) in H3 was higher than in focus area H5 (1–89 m). The reason for this may be that the data for H5 were only for four months, while the data for H3 were for two years. A reliable interpretation of the boundary movements (~1 m) in area H2 is hardly possible, because the estimated uncertainty value of our boundary change analysis is ± 1 m.

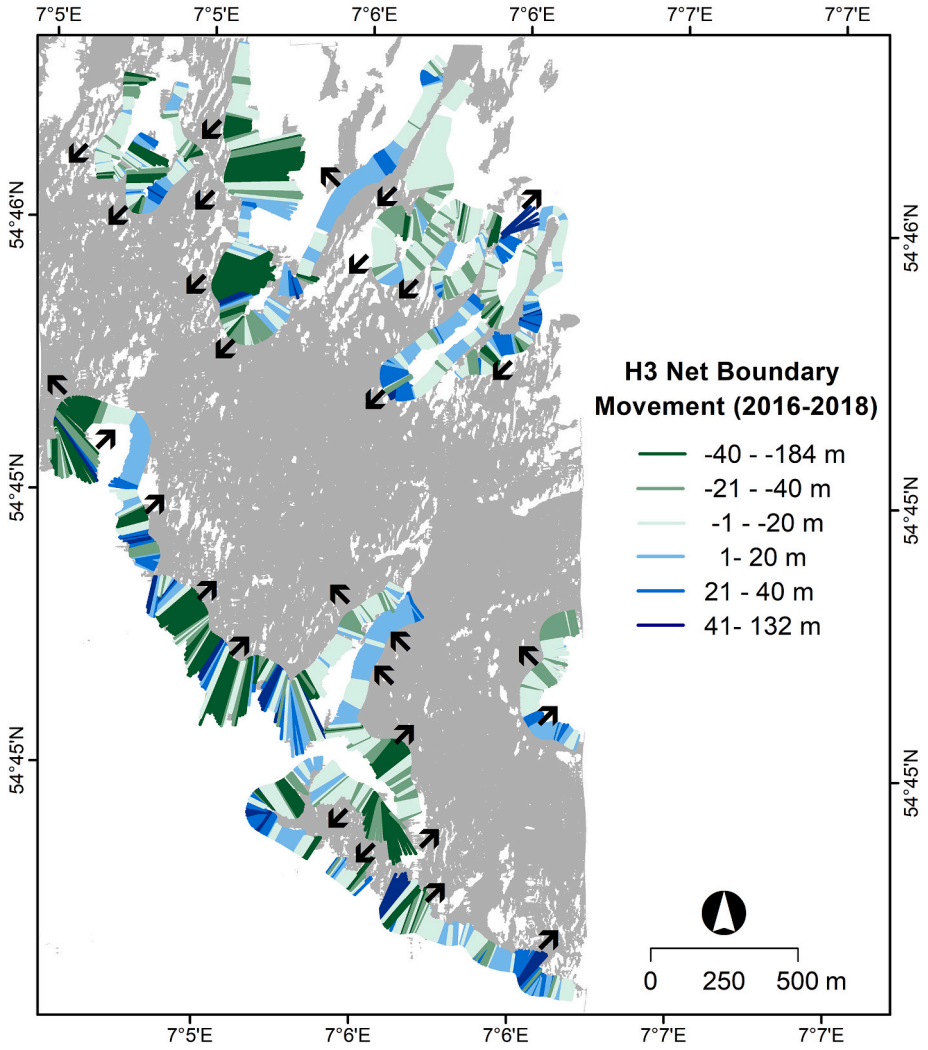

Fig. 15. Measured net boundary movement from 2016 to 2018 in H3. The boundaries seem to move towards the center of the high backscatter feature, moving from northeast to southwest.

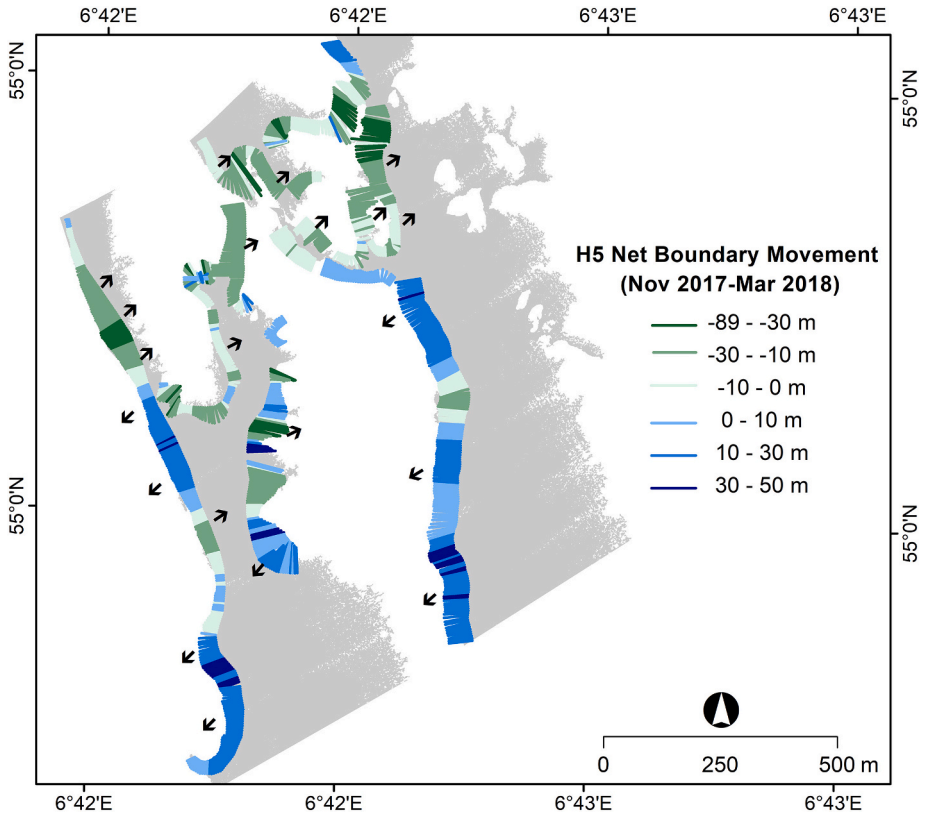

Fig. 16. Net boundary movement in H5 from Nov 2017 to Mar 2018. Advance movement was more dominant from the center to the south of the features. Boundary retreats were observed in the northern area.

Majority of the shifts were observed perpendicular to the boundary, and were directed towards the northeast and southwest orientation. The direction of movements was opposite to the direction of tidal currents in the study area, which rotates in counter-clockwise or in southeast-northwest direction (Carbajal and Pohlmann, 2004; Stanev et al., 2014). These patterns of sediment boundaries are similar to those found in previous studies of sorted bedforms in the German Bight (Diesing et al., 2006; Mielck et al., 2015). It has been suggested that movement of fine sands, driven by reversing tidal currents, can be regarded as the main process that formed and maintained the boundaries

Table 2
Summary statistics of the net boundary movement in each focus area.

	H2	H3	H5
Total number of transects:	1497	2586	1058
Maximum boundary retreat [m]:	−35.6	−183.5	−47.9
Maximum boundary advance [m]:	36.5	132.0	88.5
Percentage of boundary advances:	66.5	40.7	45.8
Percentage of boundary retreats:	33.5	59.3	54.3

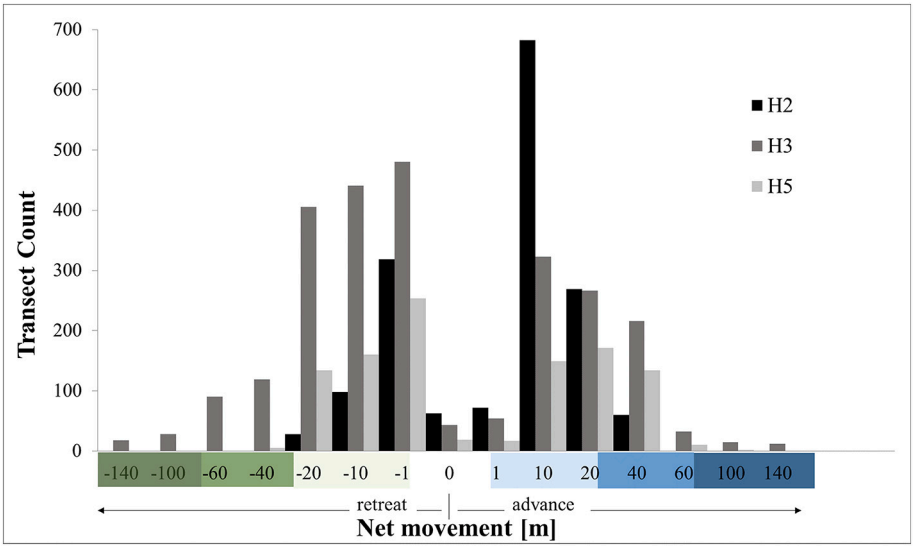

Fig. 17. Comparison of the net boundary movements in the focus areas. The Y-axis shows the number of transects, while the x-axis indicates the distance measured by these transects. The frequency distribution shows that majority of movements were less than 20 m.

(Diesing et al., 2006; Mielck et al., 2015; Murray and Thieler, 2004). However, bottom sediment characteristics do not only depend on tidal currents but also on tidal asymmetries (Stanev et al., 2014). Tidal asymmetry refers to a difference between the durations of rising and falling tides, as well as a difference in the duration and magnitude of flooding and ebbing currents (Song et al., 2011; Speer et al., 1991). A 3D-numerical model of tides in the German Bight suggests that tidal asymmetries in our study area were very sensitive to spring-neap cycles, and that it is expected that the other processes (e.g. sediment dynamics) will also be sensitive to fortnightly variations (Stanev et al., 2014). In this regard, the variations in sediment boundaries may also be a response of the seafloor sediments to tidal asymmetries.

Therefore, we presume that tidal currents and asymmetries are responsible for the mobilization of sediments along the sediment boundaries. The mobilization of sediments does not move the boundary in one direction, but instead caused gradual movement perpendicular to the current direction. This pattern may be influenced by the morphology and subsurface sediments (i.e. slope, elevation, moraine ridges), which may cause a windward-leeward effect in the sediment transport across the feature. However, additional hydrodynamic data (i.e. bottom currents) are necessary to better understand the underlying processes behind our observed trends.

6. Conclusion

In summary, we presented a workflow to process SSS data in a way that makes them fit for detailed sediment change detection analysis. Our method can be implemented in larger study areas, and is suitable for long-term monitoring programs. Moreover, the measured sediment shifts provided insights on the possible trend of sediment transport on the seafloor of the German Bight. Our findings can be used to validate sediment transport models or hydrodynamic models, and in return, can be validated by these models.

Declaration of Competing Interests

The authors declare that they have no known competing financial interests or personal relationships that could have appeared to influence the work reported in this paper.

Funding

Data of this work were generated within the project AMIN I–III (German Federal Maritime and Hydrographic Agency (BSH) [Grant no. 10038521].

Declaration of Competing Interest

None.

Acknowledgments

This research is part of the project AMIN I-III, a research and development cooperation between the Alfred-Wegener-Institute, Helmholtz Center for Polar and Marine Research (AWI) and the Federal Maritime and Hydrographic Agency in Hamburg (BSH). The project is part of a bigger project SedAWZ, coordinated by the BSH and financed by the Federal Agency for Nature Conservation (BfN). We would like to thank the crew of the research vessel ‘Heincke’.

Appendix A. Supplementary data

Supplementary data to this article can be found online at https://doi.org/10.1016/j.margeo.2020.106343.

References

Aedla, R., Dwarakish, G.S., Reddy, D.V., 2015. Automatic shoreline detection and change detection analysis of Netravati-Gurpur rivermouth using histogram equalization and adaptive thresholding techniques. Aquat. Procedia 4, 563–570. https://doi.org/10.1016/j.aqpro.2015.02.073.

Androsov, A., Fofonova, V., Kuznetsov, I., Danilov, S., Rakowsky, N., Harig, S., Brix, H., Helen Wiltshire, K., 2019. FESOM-C v.2: Coastal dynamics on hybrid unstructured meshes. Geosci. Model Dev 12, 1009–1028. https://doi.org/10.5194/gmd-12-1009-2019.

Anthony, D., Leth, J.O., 2002. Large-scale bedforms, sediment distribution and sand mobility in the eastern North Sea off the Danish west coast. Mar. Geol. 182, 247–263. https://doi.org/10.1016/S0025-3227(01)00245-6.

Armonies, W., Buschbaum, C., Hellwig-Armonies, M., 2014. The seaward limit of wave effects on coastal macrobenthos. Helgol. Mar. Res. 68, 1–16. https://doi.org/10.1007/s10152-013-0364-1.

Auster, P.J., Malatesta, R.J., Langton, R.W., Watling, L., Valentine, P.C., Donaldson, C.L.S., Langton, E.W., Shepard, A.N., Babb, I.G., 1996. The impacts of mobile fishing gear on seafloor habitats in the gulf of Maine (Northwest Atlantic): Implications for conservation of fish populations. Rev. Fish. Sci. 4, 185–202. https://doi.org/10.1080/10641269609388584.

Bera, R., Maiti, R., 2019. Quantitative analysis of erosion and accretion (1975–2017) using DSAS — a study on Indian Sundarbans. Reg. Stud. Mar. Sci. 28, 100583. https://doi.org/10.1016/j.rsma.2019.100583.

Blondel, P., 2010. The Handbook of Sidescan Sonar. Springer Science & Science Media.

BSH, 2018. GeoSeaPortal Distribution of Seabed Sediments [WWW Document]. Distrib. Seabed Sediments URL. https://www.geoseaportal.de/wss/service/SGE_SeabedSediments_1_to_10000/guest (accessed 8.20.07).

Burningham, H., French, J., 2017. Understanding coastal change using shoreline trend analysis supported by cluster-based segmentation. Geomorphology 282, 131–149. https://doi.org/10.1016/j.geomorph.2016.12.029.

Callies, U., Gaslikova, L., Kapitza, H., Scharfe, M., 2017. German Bight residual current variability on a daily basis: Principal components of multi-decadal barotropic simulations. Geo-Mar. Lett 37, 151–162. https://doi.org/10.1007/s00367-016-0466-2.

Capus, C., Ruiz, I.T., Petillot, Y., 2004. Compensation for changing beam pattern and residual tvg effects with sonar altitude variation for sidescan mosaicing and classification. In: Proc. 7th. Eur. Conf. Underw. Acoust.

Carbajal, N., Pohlmann, T., 2004. Comparison between measured and calculated tidal ellipses in the German Bight. Ocean Dyn. 54, 520–530. https://doi.org/10.1007/s10236-004-0096-5.

Cervenka, P., De Moustier, C., Lonsdale, P.F., 1994. Geometric corrections on sidescan sonar images based on bathymetry. Application with SeaMARC II and Sea Beam data. Mar. Geophys. Res. 16, 365–383. https://doi.org/10.1007/BF01203973.

Clukey, E.C., Kulhawy, F.H., Liu, P.L.F., Tate, G.B., 1985. The impact of wave loads and pore-water pressure generation on initiation of sediment transport. Geo-Mar. Lett 5, 177–183. https://doi.org/10.1007/BF02281636.

Del Río, L., Gracia, F.J., Benavente, J., 2013. Shoreline change patterns in sandy coasts. A case study in SW Spain. Geomorphology. https://doi.org/10.1016/j.geomorph.2012.07.027.

Diesing, M., Kubicki, A., Winter, C., Schwarzer, K., 2006. Decadal scale stability of sorted bedforms, German Bight, southeastern North Sea. Cont. Shelf Res. 26, 902–916. https://doi.org/10.1016/j.csr.2006.02.009.

Egbert, G.D., Erofeeva, S.Y., 2002. Efficient inverse modeling of barotropic ocean tides. J. Atmos. Ocean. Technol. 19, 183–204. https://doi.org/10.1175/1520-0426(2002)019<0183:EIMOBO>2.0.CO;2.

Eidem, E.J., Defence, N., Division, M.S., 2017. Correlation between Sediment Properties and Seafloor Characterization Maps Based on Multibeam Backscatter Data from Three Regions off the Coast. pp. 805–810.

Eriksson, B.K., van der Heide, T., van de Koppel, J., Piersma, T., van der Veer, H.W., Olff, H., 2010. Major changes in the ecology of the wadden sea: Human impacts, ecosystem engineering and sediment dynamics. Ecosystems 13, 752–764. https://doi.org/10.1007/s10021-010-9352-3.

Fakiris, E., Zoura, D., Ramfos, A., Spinos, E., Georgiou, N., Ferentinos, G., Papatheodorou, G., 2018. Object-based classification of sub-bottom profiling data for benthic habitat mapping. Comparison with sidescan and RoxAnn in a Greek shallow-water habitat. Estuar. Coast. Shelf Sci. 208, 219–234. https://doi.org/10.1016/j.ecss.2018.04.028.

Fenoglio-Marc, L., Scharroo, R., Annunziato, A., Mendoza, L., Becker, M., Lillibridge, J., 2015. Cyclone Xaver seen by geodetic observations. Geophys. Res. Lett. 42, 9925–9932. https://doi.org/10.1002/2015GL065989.

Fofonova, V., Androsov, A., Sander, L., Kuznetsov, I., Amorim, F., Christian Hass, H., Wiltshire, K.H., 2019. Non-linear aspects of the tidal dynamics in the Sylt-Rømø Bight, south-eastern North Sea. Ocean Sci. 15, 1761–1782. https://doi.org/10.5194/os-15-1761-2019.

Fonseca, L., Calder, B., 2005. Geocoder: an efficient backscatter map constructor. U.S. Hydro 2005 Conf 9.

Franzetti, M., Le Roy, P., Delacourt, C., Garlan, T., Cancouët, R., Sukhovich, A., Deschamps, A., 2013. Giant dune morphologies and dynamics in a deep continental shelf environment: Example of the banc du four (Western Brittany, France). Mar. Geol. 346, 17–30. https://doi.org/10.1016/j.margeo.2013.07.014.

Gibbons, M.J., 1988. The impact of sediment accumulations, relative habitat complexity and elevation on rocky shore meiofauna. J. Exp. Mar. Bio. Ecol. https://doi.org/10.1016/0022-0981(88)90125-6.

Goff, J.A., Mayer, L.A., Traykovski, P., Buynevich, I., Wilkens, R., Raymond, R., Glang, G., Evans, R.L., Olson, H., Jenkins, C., 2005. Detailed investigation of sorted bedforms, or “rippled scour depressions,” within the Martha’s Vineyard Coastal Observatory,

Massachusetts. Cont. Shelf Res. 25, 461–484. https://doi.org/10.1016/j.csr.2004.09.019.
Greene, A., Rahman, A.F., Kline, R., Rahman, M.S., 2018. Side scan sonar: A cost-efficient alternative method for measuring seagrass cover in shallow environments. Estuar. Coast. Shelf Sci. 207, 250–258. https://doi.org/10.1016/j.ecss.2018.04.017.
Heery, E.C., Bishop, M.J., Critchley, L.P., Bugnot, A.B., Airoldi, L., Mayer-Pinto, M., Sheehan, E.V., Coleman, R.A., Loke, L.H.L., Johnston, E.L., Komyakova, V., Morris, R.L., Strain, E.M.A., Naylor, L.A., Dafforn, K.A., 2017. Identifying the consequences of ocean sprawl for sedimentary habitats. J. Exp. Mar. Bio. Ecol. 492, 31–48. https://doi.org/10.1016/j.jembe.2017.01.020.
Himmelstoss, E.A., Henderson, R.E., Kratzmann, M.G., Farris, A.S., 2018. Digital Shoreline Analysis System (DSAS) Version 5.0 User Guide. In: Open-File Rep. 2018-1179. 126.
Ierodiaconou, D., Schimel, A.C.G., Kennedy, D., Monk, J., Gaylard, G., Young, M., Diesing, M., Rattray, A., 2018. Combining pixel and object based image analysis of ultra-high resolution multibeam bathymetry and backscatter for habitat mapping in shallow marine waters. Mar. Geophys. Res. https://doi.org/10.1007/s11001-017-9338-z.
Komar, P.D., 2010. Shoreline evolution and management of Hawke's Bay, New Zealand: Tectonics, coastal processes, and human impacts. J. Coast. Res. 26, 143–156. https://doi.org/10.2112/08-1079.1.
Korevaar, C.G., 1990. North Sea Climate: Based on Observations from Ships and LightVessels. Kluwer, Dordrecht, The Netherlands, pp. 137. https://doi.org/10.1007/978-94-009-1982-2.
Leatherman, S.P., Clow, B., 1983. UMD shoreline mapping project. IEEE Geosci. Remote Sens. Soc. Newsl. 22, 5–8.
Leiding, T., Tinz, B., Rosenhagen, G., Lefebvre, C., Haeseler, S., Hagemann, S., Bastigkeit, I., Stein, D., Schwenk, P., Müller, S., Outzen, O., 2013. Meteorological and Oceanographic conditions at the FINO platforms during the severe storms CHRISTIAN and XAVER. DEWI Mag. 16–25.
Lucas, J.S., McGlue, M.M., Kimirei, I.A., Soreghan, M.J., Mbonde, A., Yeager, K.M., Limbu, P., Apse, C., McIntyre, P.B., 2020. Geophysical benthic habitat mapping in Lake Tanganyika (Tanzania): Implications for spatial planning of small-scale coastal protected areas. J. Great Lakes Res. 46, 243–254. https://doi.org/10.1016/j.jglr.2020.01.010.
Maßmann, S., Androsov, A., Danilov, S., 2010. Intercomparison between finite element and finite volume approaches to model North Sea tides. Cont. Shelf Res. 30, 680–691. https://doi.org/10.1016/j.csr.2009.07.004.
Michaelis, R., Hass, H.C., Mielck, F., Papenmeier, S., Sander, L., Gutow, L., Wiltshire, K.H., 2019a. Epibenthic assemblages of hard-substrate habitats in the German Bight (south-eastern North Sea) described using drift videos. Cont. Shelf Res. 175, 30–41. https://doi.org/10.1016/j.csr.2019.01.011.
Michaelis, R., Hass, H.C., Papenmeier, S., Wiltshire, K.H., 2019b. Automated stone detection on side-scan sonar mosaics using haar-like features. Geosci 9. https://doi.org/10.3390/geosciences9050216.
Mielck, F., Holler, P., Bürk, D., Hass, H.C., 2015. Interannual variability of sorted bedforms in the coastal German Bight (SE North Sea). Cont. Shelf Res. 111, 31–41. https://doi.org/10.1016/j.csr.2015.10.016.
Montereale Gavazzi, G., Madricardo, F., Janowski, L., Kruss, A., Blondel, P., Sigovini, M., Foglini, F., 2016. Evaluation of seabed mapping methods for fine-scale classification of extremely shallow benthic habitats - Application to the Venice Lagoon, Italy. Estuar. Coast. Shelf Sci. 170, 45–60. https://doi.org/10.1016/j.ecss.2015.12.014.
Montereale-Gavazzi, G., Roche, M., Lurton, X., Degrendele, K., Terseleer, N., Van Lancker, V., 2018. Seafloor change detection using multibeam echosounder backscatter: Case study on the Belgian part of the North Sea. Mar. Geophys. Res. 39, 229–247. https://doi.org/10.1007/s11001-017-9323-6.
Montereale-Gavazzi, G., Roche, M., Degrendele, K., Lurton, X., Terseleer, N., Baeye, M., Francken, F., Van Lancker, V., 2019. Insights into the short-term tidal variability of multibeam backscatter from field experiments on different seafloor types. Geosci 9. https://doi.org/10.3390/geosciences9010034.
Murray, A.B., Thieler, E.R., 2004. A new hypothesis and exploratory model for the formation of large-scale inner-shelf sediment sorting and "rippled scour depressions". Cont. Shelf Res. 24, 295–315. https://doi.org/10.1016/j.csr.2003.11.001.
Otto, L., Zimmerman, J.T.F., Furnes, G.K., Mork, M., Saetre, R., Becker, G., 1990. Review of the physical oceanography of the North Sea. Netherlands J. Sea Res. 26, 161. https://doi.org/10.1016/0077-7579(90)90091-T.
Oyedotun, T.D.T., 2014. Shoreline geometry: DSAS as a tool for historical trend analysis. Geomorphol. Tech. 2, 1–12 online Ed.
Papastamatiou, Y.P., Britton, C., Burgess, G.H., 2020. Using side-scan sonar to survey critically endangered smalltooth sawfish. Fish. Res. 228, 105577. https://doi.org/10.1016/j.fishres.2020.105577.
Papenmeier, S., Hass, H.C., 2018. Detection of stones in marine habitats combining simultaneous hydroacoustic surveys. Geosci 8. https://doi.org/10.3390/geosciences8080279.
Papenmeier, S., Hass, H.C., Propp, C., Thiesen, M., Zeiler, M., 2018. Verteilung der Sedimenttypen auf dem Meeresboden in der deutschen AWZ (1:10.000) [WWW Document]. URL. www.geoseaportal.de.
Papenmeier, S., Galvez, D., Günther, C.-P., Pesch, R., Propp, C., Hass, H.C., Schuchardt, B., Zeiler, M., 2020. Winnowed gravel lag deposits between sandbanks in the German North Sea. Seafloor Geomorphol. Benthic Habitat 451–460. https://doi.org/10.1016/b978-0-12-814960-7.00025-7.
Pau, M., Hammer, T., 2013. Sediment mapping and long-term monitoring of currents and sediment fluxes in pockmarks in the Oslofjord, Norway. Mar. Geol. 346, 262–273. https://doi.org/10.1016/j.margeo.2013.09.012.
Plüß, A., 2003. Das Nordseemodell der BAW zur simulation der Tide in der Deutschen Bucht. Kuste 83–128.
Port, A., Gurgel, K.W., Staneva, J., Schulz-Stellenfleth, J., Stanev, E.V., 2011. Tidal and wind-driven surface currents in the German Bight: HFR observations versus model simulations. Ocean Dyn. 61, 1567–1585. https://doi.org/10.1007/s10236-011-0412-9.
Quality Positioning Services (QPS). 2018. *How to add a reference grid to improve backscatter corrections,* viewed January 20, 2019, < https://confluence.qps.nl/fledermaus/how-to-articles/how-to-fmgt/how-to-fmgt-add-a-reference-grid-to-improve-backscatter-corrections > .
Quality Positioning Services (QPS), 2018. FMGT Settings Menu, viewed April 20, 2020, < https://confluence.qps.nl/fledermaus7/reference-manual/fmgt/fmgt-interface/fmgt-main-menu-bar/fmgt-settings-menu > .
Quante, M., Colijin, F., 2016. North Sea Region Climate Assessment (NOSCCA). https://doi.org/10.1007/978-3-319-39745-0.
Rijnsdorp, A.D., Hiddink, J.G., van Denderen, P.D., Hintzen, N.T., Eigaard, O.R., Valanko, S., Bastardie, F., Bolam, S.G., Boulcott, P., Egekvist, J., Garcia, C., van Hoey, G., Jonsson, P., Laffargue, P., Nielsen, J.R., Piet, G.J., Sköld, M., van Kooten, T., 2020. Different bottom trawl fisheries have a differential impact on the status of the North Sea seafloor habitats. ICES J. Mar. Sci. https://doi.org/10.1093/icesjms/fsaa050.
Rosenberger, K.J., Storlazzi, C.D., Dartnell, P., 2019. Morphodynamics of a field of crescent-shaped rippled scour depressions: Northern Monterey Bay, CA. Mar. Geol. 407, 44–59. https://doi.org/10.1016/j.margeo.2018.10.006.
Rumohr, H., Kujawski, T., 2000. The impact of trawl fishery on the epifauna of the southern North Sea. ICES J. Mar. Sci. 57, 1389–1394. https://doi.org/10.1006/jmsc.2000.0930.
Schimel, A.C.G., Beaudoin, J., Gaillot, A., Keith, G., Le Bas, T., Parnum, I., Schmidt, V., 2015. Backscatter measurements by seafloor-mapping sonars - guidelines and Recommendations. In: Chapter 6 Processing Backscatter Data: From Datagrams to Angular Responses and Mosaics, pp. 133–164.
Song, D., Wang, X.H., Kiss, A.E., Bao, X., 2011. The contribution to tidal asymmetry by different combinations of tidal constituents. J. Geophys. Res. Ocean. 116, 1–12. https://doi.org/10.1029/2011JC007270.
Soulsby, R.L., Hamm, L., Klopman, G., Myrhaug, D., Simons, R.R., Thomas, G.P., 1993. Wave-current interaction within and outside the bottom boundary layer. Coast. Eng. 21, 41–69. https://doi.org/10.1016/0378-3839(93)90045-A.
Speer, P.E., Aubrey, D.G., Friedrichs, C.T., 1991. Nonlinear hydrodynamics of shallow tidal inlet/bay systems. Tidal Hydrodyn. 321–339.
Stammer, D., Ray, R.D., Andersen, O.B., Arbic, B.K., Bosch, W., Carrère, L., Cheng, Y., Chinn, D.S., Dushaw, B.D., Egbert, G.D., Erofeeva, S.Y., Fok, H.S., Green, J.A.M., Griffiths, S., King, M.A., Lapin, V., Lemoine, F.G., Luthcke, S.B., Lyard, F., Morison, J., Müller, M., Padman, L., Richman, J.G., Shriver, J.F., Shum, C.K., Taguchi, E., Yi, Y., 2014. Accuracy assessment of global barotropic ocean tide models. Rev. Geophys. https://doi.org/10.1002/2014RG000450.Received.
Stanev, E.V., Al-Nadhairi, R., Staneva, J., Schulz-Stellenfleth, J., Valle-Levinson, A., 2014. Tidal wave transformations in the German Bight. Ocean Dyn. 64, 951–968. https://doi.org/10.1007/s10236-014-0733-6.
Staneva, J., Stanev, E.V., Wolff, J.O., Badewien, T.H., Reuter, R., Flemming, B., Bartholomä, A., Bolding, K., 2009. Hydroynamics and sediment dynamics in the German Bight. A focus on observations and numerical modelling in the East Frisian Wadden Sea. Cont. Shelf Res. 29, 302–319. https://doi.org/10.1016/j.csr.2008.01.006.
Staneva, J., Wahle, K., Günther, H., Stanev, E., 2016. Coupling of wave and circulation models in coastal-ocean predicting systems: A case study for the German Bight. Ocean Sci. 12, 797–806. https://doi.org/10.5194/os-12-797-2016.
Subarsyah, S., Arifin, L., 2019. Seabed characterization through image processing of side scan sonar case study: Bontang and Batam. Bull. Mar. Geol. 34.
Thieler, R.E., Himmelstoss, E.A., Zichichi, J.L., Ergul, A., 2017. Digital Shoreline Analysis System (DSAS) Version 4.0–an ArcGIS Extension for Calculating Shoreline Change (ver. 4.4, July 2017).
Thistle, D., Yingst, J.Y., Fauchald, K., 1985. A deep-sea benthic community exposed to strong near-bottom currents on the Scotian Rise (western Atlantic). Mar. Geol. 66, 91–112.
Trimble, 2019. Specifications Trimble SPS461 Modular GPS Heading Receiver Trimble SPS461 Modular GPS Heading Receiver [WWW Document]. URL http://allterra-dno.de/wp-content/uploads/2017/09/SPS_Master_Specs_SPS461-RTK.pdf. (Accessed 07 July 2019).
Troell, M., Pihl, L., Rönnbäck, P., Wennhage, H., Söderqvist, T., Kautsky, N., 2005. Regime shifts and ecosystem services in Swedish coastal soft bottom habitats: When resilience is undesirable. Ecol. Soc. 10. https://doi.org/10.5751/ES-01374-100130.
United States Geological Survey, (USGS), 2019. Digital Shoreline Analysis System [WWW Document]. URL. https://code.usgs.gov/cch/dsas.

Van Lancker, V., Baeye, M., 2015. Wave glider monitoring of sediment transport and dredge plumes in a shallow marine sandbank environment. PLoS One 10, 1–19. https://doi.org/10.1371/journal.pone.0128948.

Van Lancker, V., Lanckneus, J., Hearn, S., Hoekstra, P., Levoy, F., Miles, J., Moerkerke, G., Monfort, O., Whitehouse, R., 2004. Coastal and nearshore morphology, bedforms and sediment transport pathways at Teignmouth (UK). Cont. Shelf Res. 24, 1171–1202. https://doi.org/10.1016/j.csr.2004.03.003.

Zeiler, M., Schulz-Ohlberg, J., Figge, K., 2000. Mobile sand deposits and shoreface sediment dynamics in the inner German Bight (North Sea). Mar. Geol. 170, 363–380. https://doi.org/10.1016/S0025-3227(00)00089-X.

Zeiler, M., Schwarzer, K., Ricklefs, K., 2008. Seabed morphology and sediment dynamics. Kuste 31–44.

Zhao, J., Yan, J., Zhang, H., Meng, J., 2017. A new radiometric correction method for side-scan sonar images in consideration of seabed sediment variation. Remote Sens. 9. https://doi.org/10.3390/rs9060575.